arXiv:1701.03314v2 [stat.ME] 24 Jan 2017

Positive-Definite Multivariate Spectral Estimation: A Geometric Wavelet Approach

Joris Chau* and Rainer von Sachs†

Abstract

In nonparametric estimation of the autocovariance matrices or the spectral density matrix of a second-order stationary multivariate time series, it is important to preserve positive-definiteness of the estimator. This in order to ensure interpretability of the estimator as a covariance or spectral matrix, but also to avoid computational issues in e.g. simulation or bootstrapping. To this purpose, we consider multivariate spectral estimation on the Riemannian manifold of Hermitian and positive-definite matrices – based on a geometric wavelet approach. Nonlinear wavelet curve denoising on the Riemannian manifold allows one to capture not only local smoothness behavior in the spectral matrix across frequency, but also varying degrees of smoothness across components of the spectral matrix. Moreover, and in contrast to existing approaches, the wavelet-based spectral estimator enjoys the important property that it is equivariant to permutations of the components of the time series. In addition to spectral estimation, we propose computationally fast clustering of spectral matrices based on their wavelet domain representations, exploiting the fact that smooth curves on the Riemannian manifold are summarized by few high-energy wavelet coefficients. The spectral estimation and clustering methods are applied to analyze a brain signal time series dataset recorded over the course of an associative learning experiment.

Keywords: Riemannian manifold, Hermitian positive-definite matrices, Manifold wavelet transform, Wavelet thresholding, Cluster analysis, Multivariate time series.

1 Introduction

In multivariate time series analysis, the second-order behavior of a multivariate time series is studied by means of the autocovariance matrices in the time domain, or the spectral density matrix in the frequency domain. A non-degenerate spectral density matrix is necessarily a curve of Hermitian positive-definite (PD) matrices, and one generally constrains a spectral curve estimator to preserve these properties. This is important for several reasons: i) interpretation of the spectral estimator as the Fourier transform of autocovariance matrices of the time series; ii) well-defined transfer functions in the Cramér representation of the

*Corresponding author, j.chau@uclouvain.be, Institute of Statistics, Biostatistics, and Actuarial Sciences (ISBA), Université catholique de Louvain, Voie du Roman Pays 20, B-1348, Louvain-la-Neuve, Belgium.

†Institute of Statistics, Biostatistics, and Actuarial Sciences (ISBA), Université catholique de Louvain, Voie du Roman Pays 20, B-1348, Louvain-la-Neuve, Belgium.

time series for the purpose of e.g. simulation of time series observations or bootstrapping; iii) sufficient regularity to avoid any computational problems in subsequent inference procedures (requiring e.g. the inverse of the estimated spectrum). Our contribution is to develop a natural framework for multivariate spectral anlaysis in the space of Hermitian PD matrices by exploiting its geometric structure as a Riemannian manifold. In this work we focus primarily on spectral density matrix estimation, but we emphasize that the methodology applies to general matrix-valued curve estimation problems, where the target is a curve of symmetric or Hermitian PD matrices. As an example, we cite estimation of time-varying autocovariance matrices of a locally stationary time series (see [6]), where the time-varying autocovariance matrices constitute a curve of symmetric PD matrices over time. Below, we formalize the approach in the specific situation of nonparametric spectral density matrix estimation in the context of stationary multivariate time series.

Let $\vec{Y}(t) := (Y_1(t), \ldots, Y_d(t))'$ be a d-dimensional second-order jointly stationary time series, where it is assumed that the time series has zero mean (otherwise recenter the time series to have zero mean). If for each $-\infty < h < \infty$ the autocovariance functions $\Gamma(h) = \boldsymbol{E}[\vec{Y}(t+h)\vec{Y}'(t)]$ have absolutely summable components, i.e. $\sum_{h=-\infty}^{\infty} |\Gamma_{ij}(h)| < \infty$, $\forall i, j = 1, \ldots, d$, the spectral density matrix of $\vec{Y}(t)$ exists and is given by the componentwise Fourier transform of the autocovariance functions:

$$f(\omega) \quad = \quad \frac{1}{2\pi} \sum_{h=-\infty}^{\infty} \Gamma(h) e^{-ih\omega}, \qquad -\pi \leq \omega \leq \pi$$

A non-degenerate spectral density matrix $f(\omega)$ is Hermitian and positive-definite at each frequency $\omega \in [-\pi, \pi]$, see [3]. Given discrete time series observations $(\vec{Y}(1), \ldots, \vec{Y}(T))$, a nonparametric estimator of $f(\omega)$ at the Fourier frequencies $\omega_\ell = 2\pi\ell/T$, with $-[(T-1)/2] \leq \ell \leq [T/2]$, is given by the periodogram:

$$I_T(\omega_\ell) \quad = \quad \vec{J}(\omega_\ell)\vec{J}^*(\omega_\ell)$$

where $\vec{J}(\omega_\ell) = \frac{1}{\sqrt{T}} \sum_{t=1}^{T} \vec{Y}(t) e^{-it\omega_\ell}$ is the discrete Fourier transform of the vector of time series observations, and * denotes the conjugate transpose. The periodogram $I_T(\omega_\ell)$ is an asymptotically unbiased, but inconsistent estimator of the spectrum $f(\omega_\ell)$. Moreover, it is not positive-definite, as the rank of $I_T(\omega_\ell)$ is one. Several straightforward ways to obtain positive-definite and consistent estimators of the spectral matrix include: smoothing (locally weighted averaging) of the periodogram over frequency, or multitaper spectral estimation, a generalization of Welch's method using orthogonal tapering functions (see [28]).

If the matrix components in the spectral matrix $f(\omega)$ share the same degree of (sufficiently) smooth behavior over frequency, then the above methods to obtain a Hermitian PD spectral estimator generally perform well. However, if the elements in the spectral matrix do not share the same degrees of smoothness, these approaches may perform poorly – this is

demonstrated by several simulated examples in the appendix. To illustrate this issue with a practical example, consider multivariate spectral estimation of local field potential (LFP) brain signal data as in Section 5. In this LFP dataset, as demonstrated in Figure 6, the auto-spectra contain pronounced peaks, whereas the cross-spectra are highly smooth curves over frequency. If the periodogram is smoothed over frequency identically across matrix components, we either smooth out the peaks in the auto-spectral components, or we under-smooth the nearly constant curves in the cross-spectral components. On the other hand, if the periodogram is smoothed over frequency with different (local) smoothing bandwidths for different components of the spectral matrix, positive-definiteness of the resulting finite-sample estimator cannot be guaranteed. To address this issue, the approach in [7], [23], and [17] is to smooth individual components of the Cholesky square root matrices of the spectrum, as a consequence, the square of the smoothed estimator is automatically a Hermitian PD spectral estimator. Unfortunately, Cholesky-based smoothing is not necessarily equivariant to permutations of the components of the underlying time series. By this we mean the following, if one observes a reordering of the components of the time series, the spectral matrix of the reordered time series is equal to the original spectral matrix up to a permutation of the matrix elements. It is desirable for the spectral estimator to satisfy this property as well, i.e. the spectral estimator of a reordered time series should be invariant up to permutation of the elements of the estimated spectral matrix.

In this work, we propose to solve this curve denoising problem via a wavelet approach from a geometric point of view, which to the best of our knowledge has not been applied to this type of multivariate smoothing problems. The space of Hermitian PD matrices is a symmetric differentiable Riemannian manifold, and the spectral matrix $f(\omega)$ is a curve along frequency on the manifold. Instead of embedding the set of Hermitian PD matrices in a Euclidean space, we consider wavelet-based curve-denoising of the periodogram matrix on a Riemannian manifold. The constructed wavelet transform is based on a specific *natural* Riemannian distance function, which in many ways leads to a more natural measure of distance or closeness between Hermitian PD matrices than their Euclidean distance, (see also [2], [21], or [24]). To illustrate with an example, the Riemannian distance function transforms the metric manifold into a regular and complete metric space, whereas the space of Hermitian PD matrices combined with the Euclidean metric is an incomplete metric space, as there is a boundary at a finite distance. Also, determinants (or volumes) of matrices on a connecting shortest line segment with respect to the Riemannian distance function are always bounded by the determinants of the segment endpoints, which is generally not the case for determinants of matrices on a shortest line segment with respect to the Euclidean distance.

Motivated from classical wavelet methodology, the manifold wavelet transform is constructed through local geometric averages and differences of points in the space of Her-

mitian PD matrices based on the Riemannian distance function. Consequently, nonlinear thresholding or shrinkage of coefficients of the wavelet-transformed periodogram matrix enables us to capture different degrees of smoothness of curves across components of the spectral matrix as in the Cholesky-based methods, and since the wavelet-denoised spectral estimator is necessarily a curve on the manifold, it is always Hermitian and positive-definite. Moreover, and in contrast to the Cholesky-based methods, due to the geometric nature of the spectral estimator it is equivariant to permutations of the components of the time series. We are interested in a wavelet-based approach because, on the one hand, wavelets allow us to benefit from the spatial adaptivity of nonlinear smoothing of curves towards localized features (such as local peaks and troughs in the spectrum). On the other hand, nonlinear wavelet thresholding provides for sparse representations of the spectral matrix in the wavelet domain. The latter can also be exploited for other purposes than curve estimation, such as computationally fast clustering of spectral matrices. This is developed in the second part of the paper.

The structure of the paper is as follows. In Section 2 we introduce the necessary geometric notions and tools, and outline the midpoint-interpolation forward and backward wavelet transform on the Riemannian manifold of Hermitian PD matrices. In Section 3 we present the spectral estimation procedure based on nonlinear thresholding of the wavelet coefficients of a pre-smoothed periodogram matrix. We consider hard thresholding of components in an orthonormal basis of the matrix-valued wavelet coefficients, where the threshold is automatically selected via a cross-validation procedure, and we show that the wavelet-thresholded estimator of the spectrum is equivariant to permutations of the components of the time series. In Section 4 we detail an additional application of the proposed methodology: computationally fast clustering of spectral matrices in the wavelet domain. Again, the ordering of the components of the time series does not play a role, as the cluster assignments are exactly equivalent under any reordering of the components. In Section 5 we apply the developed methodology to analyze a brain signal data example consisting of local field potential time series recorded over the course of an associative learning experiment. The technical proofs are deferred to the appendix, and the accompanying `R`-code providing the tools to perform fully automatic wavelet-based multivariate spectral estimation and clustering is publicly available in the `R`-package `pdSpecEst` on CRAN, [4].

2 Preliminaries

The set $\mathcal{M} := \mathbb{P}_{d\times d}$ of $(d \times d)$-dimensional Hermitian PD matrices is a well-studied symmetric, differentiable Riemannian manifold (see e.g. [2] or [20]). The tangent space $\mathcal{T}_P(\mathcal{M})$ at a point, i.e. a matrix, $P \in \mathcal{M}$ can be identified by the real vector space $\mathcal{H} := \mathbb{H}_{d\times d}$ of $(d \times d)$-dimensional Hermitian matrices, and the inner product on $\mathcal{H}$ leads to the *natural*

(also invariant, Fisher information, or Fisher-Rao) Riemannian metric on the manifold $\mathcal{M}$ given by the family of inner products:

$$\langle H_1, H_2 \rangle_p \quad = \quad \mathrm{Tr}(P^{-1/2} H_1 P^{-1} H_2 P^{-1/2}), \qquad \text{for each } P \in \mathcal{M}$$

with $H_1, H_2 \in \mathcal{H}$. Here and throughout the document, $P^{1/2}$ denotes the Hermitian square root matrix of $P \in \mathcal{M}$. The natural Riemannian distance on $\mathcal{M}$ derived from the Riemannian metric is given by:

$$\delta(P_1, P_2) \;=\; \delta(P_2, P_1) \quad = \quad \|\mathrm{Log}(P_1^{-1} P_2)\|_F \tag{2.1}$$

By [2, Prop. 6.2.2], it follows that $(\mathcal{M}, \delta)$ is a complete metric space, which by the Hopf-Rinow Theorem implies that each geodesic curve can be extended indefinitely. Note that singular matrices are pushed to the boundary of the metric space $(\mathcal{M}, \delta)$ in the sense that the distance from a point in $\mathcal{M}$ to any singular matrix is infinity. In contrast, the space of Hermitian PD matrices embedded in the Euclidean space $\mathbb{R}^{d^2}$ is an incomplete metric space, since the boundary of singular matrices lies at a finite distance.
The Riemannian distance (as the Riemannian metric) is invariant under congruence transformation by the general linear group of $d \times d$-dimensional matrices $\mathrm{GL}(d, \mathbb{C})$, where by congruence transformation we refer to the mapping $X \mapsto g * X$, using the notation $g * X := g^* X g$, with $X \in \mathcal{M}$ and $g \in \mathrm{GL}(d, \mathbb{C})$. That is,

$$\delta(P_1, P_2) \quad = \quad \delta(g * P_1, g * P_2), \qquad \text{for any } g \in \mathrm{GL}(d, \mathbb{C})$$

By [2, Theorem 6.1.6], the shortest curve with respect to the Riemannian distance function, i.e. the geodesic, joining any two points $P_1, P_2 \in \mathcal{M}$ is unique and can be parametrized as:

$$\gamma(P_1, P_2, t) \quad = \quad P_1^{1/2} * \left(P_1^{-1/2} * P_2 \right)^t, \qquad 0 \le t \le 1 \tag{2.2}$$

The midpoint between two points in $\mathcal{M}$ is defined as the midpoint of the unique geodesic connecting the points, i.e. $\mathrm{Mid}(P_1, P_2) = \gamma(P_1, P_2, 1/2)$. Furthermore, given a point P_1 and some midpoint $P_{1\#2} = \mathrm{Mid}(P_1, P_2)$, the endpoint P_2 on the extended geodesic trough P_1 and $P_{1\#2}$ is retrieved as $P_2 = P_{1\#2} * P_1^{-1}$.

The exponential maps $\mathrm{Exp}_P : \mathcal{T}_P(\mathcal{M}) \simeq \mathcal{H} \to \mathcal{M}$ are diffeomorphic maps from the tangent space attached at a point $P \in \mathcal{M}$ to the manifold and are given by:

$$\mathrm{Exp}_P(H) \quad = \quad P^{1/2} * \mathrm{Exp}\left(P^{-1/2} * H \right)$$

where $\mathrm{Exp}(\cdot)$ is the matrix exponential. Since the matrices under consideration are always Hermitian and therefore diagonalizable, the matrix exponential of a Hermitian matrix $H = UDU^{-1}$, with D a diagonal matrix, is given by $\mathrm{Exp}(H) = U \exp(D) U^{-1}$, where $\exp(D)$ exponentiates each entry on the diagonal of D. Since $\mathcal{M}$ is a geodesically complete manifold

and the minimizing geodesics are always unique, it follows by [8, Chapter 13] that for each $P \in \mathcal{M}$ the image of the exponential map Exp_P is the entire manifold $\mathcal{M}$, (i.e. there is no cut-locus). This implies that the exponential maps are *global* diffeomorphisms. In the other direction, the logarithmic maps are global diffeomorphic maps from the manifold to the tangent space attached at a point $P \in \mathcal{M}$, and are defined as the unique inverse exponential maps $\mathrm{Log}_P(\tilde{P}) : \mathcal{M} \to \mathcal{T}_P(\mathcal{M})$ given by:

$$\mathrm{Log}_P(\tilde{P}) \quad = \quad P^{1/2} * \mathrm{Log}\left(P^{-1/2} * \tilde{P}\right)$$

where $\mathrm{Log}(\cdot)$ is the matrix logarithm. For a Hermitian matrix $H = UDU^{-1}$, with D a diagonal matrix, the matrix logarithm of H is given by $\mathrm{Log}(H) = U \log(D) U^{-1}$, where $\log(D)$ takes the logarithm of each entry on the diagonal of D.

2.1 Manifold wavelet transform

In order to construct a wavelet transform on the manifold of Hermitian PD matrices, we consider a modified version of the *midpoint-interpolation* (MI) approach developed in [22] for general symmetric Riemannian manifolds with tractable exponential and logarithmic maps. The MI approach is essentially a generalization of the average-interpolation (AI) wavelet transform on the real line, see [9], to the Riemannian manifold $\mathcal{M}$. We emphasize that such procedures are closely related to the idea of *lifting* wavelet transforms, see e.g. [14] for a general overview of (second-generation) wavelet transforms using the lifting scheme.

2.1.1 MI refinement scheme on a bounded interval

With in mind the application to spectral matrices, we consider a discretized curve $f(\omega_\ell) \in \mathcal{M}$ at equidistant frequency points $\omega_\ell \in \mathcal{I}$ for $\ell = 1, \ldots, n$, with $\mathcal{I} \subset \mathbb{R}$, such as $\mathcal{I} = (0, \pi]$. Here, we assume that $n = 2^J$ is a power of two in order to avoid problems in the subsequent construction of the wavelet transforms. Note that this is not an absolute limitation of the approach, as we can extend it for non-dyadic values of n. Given the sequence $(f(\omega_\ell))_\ell$, we build a midpoint pyramid with values $M_{j,k} \in \mathcal{M}$ for $j = 1, \ldots, J$ and $k = 0, \ldots, 2^j - 1$. At the finest scale J, we start by setting,

$$M_{J,k} \quad = \quad f(\omega_{k+1}), \qquad \text{for } k = 0, \ldots, 2^J - 1$$

At the next coarser scale $j = J - 1$ we put,

$$M_{j,k} \quad = \quad \mathrm{Mid}(M_{j+1,2k}, M_{j+1,2k+1}), \qquad \text{for } k = 0, \ldots, 2^j - 1 \tag{2.3}$$

We continue this coarsening operation up to scale $j = 1$, such that each scale $j = 1, \ldots, J$ contains a total of 2^j midpoints.

At scale $j \in \{1, \ldots, J-1\}$, the MI refinement scheme takes as input the midpoints

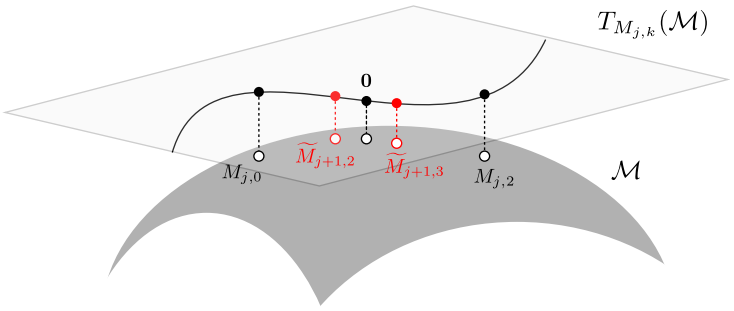

Figure 1: Illustration of the midpoint-interpolation refinement scheme on a 2d-surface.

$(M_{j,k})_{k=0,\dots,2^j-1}$ and outputs imputed or predicted midpoints $(\widetilde{M}_{j+1,k})_{k=0,\dots,2^{j+1}-1}$. This involves the following steps:

1. Fix an odd integer $N = 2D+1$, with $D \in \mathbb{N}_0$, corresponding to the order of the refinement scheme. In order to compute the imputed midpoints $\widetilde{M}_{j+1,2k}$ and $\widetilde{M}_{j+1,2k+1}$ at scale $j+1$, if available collect the set of N midpoints closest to $M_{j,k}$ at scale j, i.e. the set $\{M_{j,k-D}, \dots, M_{j,k}, \dots, M_{j,k+D}\}$. For the special case $D = 0$, instead of collecting just a single midpoint $M_{j,k}$, collect either the set $\{M_{j,k}, M_{j,k+1}\}$ or $\{M_{j,k-1}, M_{j,k}\}$ whichever is available. This is essential in reconstructing geodesic curves requiring interpolation of *at least* two adjacent midpoints, see also the Remark below.

2. Transform the collected midpoints $\{M_{j,k-D}, \dots, M_{j,k}, \dots, M_{j,k+D}\}$ to the tangent space $\mathcal{T}_{M_{j,k}}(\mathcal{M}) \simeq \mathcal{H}$ via the logarithm map, which is a global diffeomorphism:

$$\Theta_{j,k+\ell} \;=\; \mathrm{Log}_{M_{j,k}}(M_{j,k+\ell}), \qquad -D \le \ell \le D$$

   Note that $\mathrm{Log}_{M_{j,k}}(M_{j,k}) = \mathbf{0}_{d\times d}$ the zero matrix corresponding to the identity element in $\mathcal{H}$. The space of $d \times d$-dimensional Hermitian matrices $\mathcal{H}$ is a real vector space, therefore we can decompose each Hermitian matrix $\Theta_{j,k+\ell}$ with respect to an orthonormal (in terms of $\langle\cdot,\cdot\rangle_F$) basis $(E_i)_{i=1,\dots,d^2}$ as:

$$\Theta_{j,k+\ell} \;=\; \sum_{i=1}^{d^2} \theta^i_{j,k+\ell} E_i, \qquad -D \le \ell \le D$$

3. Since the sequences $\theta^i_{j,k+\ell} = \langle \Theta_{j,k+\ell}, E_i\rangle_F$ with $-D \le \ell \le D$ are real-valued, we can apply classical average-interpolation refinement as in [9] to find the imputed values $\tilde{\theta}^i_{j+1,2k}, \tilde{\theta}^i_{j+1,2k+1} \in \mathbb{R}$ for each $i = 1, \dots, d^2$. The imputed midpoints $\widetilde{M}_{j+1,2k}$ and $\widetilde{M}_{j+1,2k+1}$ are then found by transforming the imputed points in the tangent space $\mathcal{T}_{M_{j,k}}(\mathcal{M})$ back to the manifold via the exponential map:

$$\widetilde{M}_{j+1,2k} \;=\; \mathrm{Exp}_{M_{j,k}}\left(\sum_{i=1}^{d^2} \tilde{\theta}^i_{j+1,2k} E_i\right), \qquad \widetilde{M}_{j+1,2k+1} \;=\; \mathrm{Exp}_{M_{j,k}}\left(\sum_{i=1}^{d^2} \tilde{\theta}^i_{j+1,2k+1} E_i\right)$$

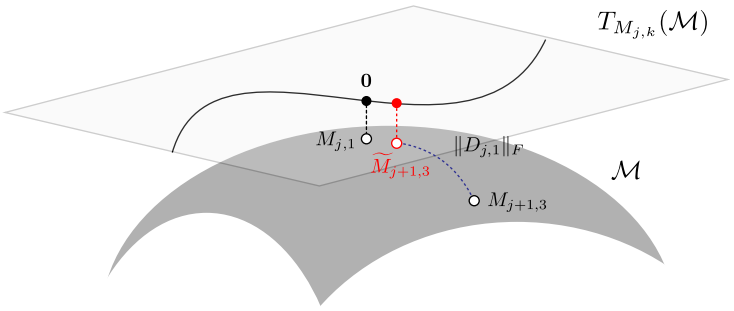

Figure 2: Illustration of (construction of) wavelet coefficients on a 2d-surface.

Given midpoints $(M_{j,k})_{k=0,\ldots,2^j-1}$ and the order of the refinement scheme N, this procedure results in imputed midpoints $(\widetilde{M}_{j+1,k})_{k=0,\ldots,2^{j+1}-1}$ at the next coarser scale for each $j = 1,\ldots,J-1$. As in a classical average-interpolation refinement scheme, close to the left and right boundaries of the observation interval, the order of the refinement scheme gradually decreases taking into account only right of left neighboring midpoints at the boundaries.

Remark The reason we build the midpoint pyramid up to coarsest scale $j = 1$, instead of scale $j = 0$, is that we wish to always be able to reconstruct geodesic curves. However, this requires *at least* two neighboring midpoints to exist on a given scale j in the MI refinement scheme, otherwise the geodesic curve cannot be uniquely identified.

2.1.2 MI forward and backward wavelet transform

The MI refinement scheme leads to an MI wavelet transform passing from fine-scale midpoints at scale $j+1$ to coarse-scale midpoints plus wavelet coefficients at scale j as follows:

1. **Coarsen/Predict:** given midpoints $(M_{j+1,k})_{k=0,\ldots,2^{j+1}-1}$ at scale $j+1$, compute the midpoints $(M_{j,k})_{k=0,\ldots,2^j-1}$ at scale j through the midpoint relation in eq.(2.3) and generate the imputed midpoints $(\widetilde{M}_{j+1,k})_{k=0,\ldots,2^{j+1}-1}$ based on the coarse-scale midpoints.

2. **Difference:** given true and imputed midpoints $M_{j+1,2k+1}, \widetilde{M}_{j+1,2k+1}$, define the wavelet coefficients as a *difference in the tangent space* according to,

$$D_{j,k} \quad = \quad \mathrm{Log}(\widetilde{M}_{j+1,2k+1}^{-1/2} * M_{j+1,2k+1}) \in \mathcal{T}_{\mathrm{I}_d}(\mathcal{M})$$

   Note that $\|D_{j,k}\|_F = \delta(M_{j+1,2k+1}, \widetilde{M}_{j+1,2k+1})$ by definition of the Riemannian distance function, giving the wavelet coefficients the interpretation of a difference between $M_{j+1,2k+1}$ and $\widetilde{M}_{j+1,2k+1}$.

The backward wavelet transform passing from coarse-scale midpoints plus wavelet coefficients at scale j to fine-scale midpoints at scale $j+1$, follows directly from reverting the above operations:

1. **Predict/Refine**: given midpoints $(M_{j,k})_{k=0,\ldots,2^j-1}$, generate the imputed midpoints $(\widetilde{M}_{j+1,k})_{k=0,\ldots,2^{j+1}-1}$, and compute the fine-scale midpoints at the odd locations $2k+1$ for $k = 0, \ldots, 2^j - 1$ through:

$$M_{j+1,2k+1} \quad = \quad \widetilde{M}_{j+1,2k+1} * \mathrm{Exp}(D_{j,k})$$

2. **Complete**: since the coarse-scale midpoints satisfy the midpoint relation $M_{j,k} = \mathrm{Mid}(M_{j+1,2k}, M_{j+1,2k+1})$, using the fine-scale midpoints at the odd locations $M_{j+1,2k+1}$ from the previous step, we retrieve the fine-scale midpoints at the even locations by extending the geodesic through $M_{j+1,2k+1}$ and $M_{j,k}$ via:

$$M_{j+1,2k} \quad = \quad M_{j,k} * M_{j+1,2k+1}^{-1}$$

Given the midpoints $(M_{1,k})_k$ at scale $j = 1$ and the pyramid of wavelet coefficients $(D_{j,k})_{j,k}$, repeating the reconstruction procedure above until the finest scale, we retrieve the original discretized curve $M_{J,k} = f(\omega_{k+1})$ for $k = 0, \ldots, 2^J - 1$.

3 Periodogram matrix denoising

Consider again a d-dimensional zero-mean stationary observed time series with spectrum $f(\omega)$ and periodogram $I_n(\omega_\ell)$ at the Fourier frequencies $\omega_\ell = 2\pi\ell/n \in (0, \pi]$ for $\ell = 1, \ldots, n$. By [7, Lemma 1], for $\omega_\ell \not\equiv 0 \pmod{\pi}$, the multitaper spectral estimates $\hat{f}_n(\omega_\ell)$, with a fixed number of tapers B, are asymptotically independent at the Fourier frequencies, and their asymptotic distribution satisfies:

$$\hat{f}_n(\omega_\ell) \quad \xrightarrow{d} \quad W_d^c(B, B^{-1}f(\omega_\ell)), \qquad \text{as } n \to \infty$$

where $W_d^c(B, B^{-1}f(\omega_\ell))$ is a complex Wishart distribution of dimension d with B degrees of freedom. The same holds true approximately for a locally averaged periodogram $\hat{f}_n(\omega_\ell) = \frac{1}{B}\sum_{i=-\lceil B/2\rceil+1}^{\lfloor B/2\rfloor} I_n(\omega_{\ell+i})$. If $B \geq d$, then the spectral estimate $\hat{f}_n(\omega_\ell)$ is Hermitian and positive-definite with probability one, i.e. $\hat{f}_n(\omega_\ell) \in \mathcal{M}$ almost surely. In practice, we wish to choose B as small as possible, preferably $B = d$, so that only the necessary small amount of smoothing is performed to guarantee a positive-definite initial spectral estimator. In this way, the essential curve denoising operation consists of shrinking or thresholding wavelet coefficients in the manifold wavelet domain capturing inhomogeneous local smoothness across different components of the spectral matrix, which cannot be done by the initial smoothing parameter B.

3.1 Asymptotic bias-correction

Let $X \sim W_d^c(B, B^{-1}f)$ with $B \geq d$, then X is a random variable (random matrix) on the manifold $\mathcal{M}$ of Hermitian PD matrices, below we also write P_f for the probability

distribution of X on the manifold $\mathcal{M}$. The Euclidean expectation of X equals f and can be expressed as the value in $\mathcal{M}$ that minimizes the variance in terms of the Euclidean (i.e. Frobenius) norm under the distribution P_f,

$$\boldsymbol{E}[X] \;=\; f \;=\; \arg\min_{m\in\mathcal{M}} \int_{\mathcal{M}} \|X-m\|_F^2 \; dP_f(X)$$

Given $X_1,\ldots,X_n \overset{\text{iid}}{\sim} W_d^c(B,B^{-1}f)$, the ordinary arithmetic mean $\frac{1}{n}\sum_{\ell=1}^n X_\ell$ is then an unbiased and consistent estimator of f as $n\to\infty$. Averaging in the midpoint pyramid is performed through repeated application of the midpoint operator, thereby calculating a geometric mean on the manifold. If $n=2^J$ for some $J>0$, then we define the repeated midpoint functional as in [22] recursively as:

$$\mu_n(X_1,\ldots,X_n) \;=\; \text{Mid}\left(\mu_{n/2}(X_1,\ldots,X_{n/2}),\mu_{n/2}(X_{n/2+1},\ldots,X_n)\right)$$

The repeated midpoint functional converges to a limit as $n\to\infty$, but it does not converge to the Euclidean expectation $\boldsymbol{E}[X_\ell]=f$, since it is not based on the Euclidean metric. Instead, μ_n converges to a Karcher (or Fréchet) expectation, which can be characterized as the point on the manifold that minimizes the variance in terms of the Riemannian distance under the distribution P_f,

$$\mathbb{E}[X] \;=\; \arg\min_{m\in\mathcal{M}} \boldsymbol{E}[\delta(X,m)^2] \;=\; \arg\min_{m\in\mathcal{M}} \int_{\mathcal{M}} \delta(X,m)^2 \; dP_f(X) \tag{3.1}$$

assuming that $\boldsymbol{E}[\delta(X,m)^2]<\infty$ for all $m\in\mathcal{M}$. By [20], we know that on $\mathcal{M}$, a manifold without cut-locus, the Karcher mean $\mu:=\mathbb{E}[X]$ exists and is unique. Recall that the cut-locus at a point $P\in\mathcal{M}$ is the complement of the image of the exponential map Exp_P, which is the empty set for each $P\in\mathcal{M}$ as the image of Exp_P is the entire manifold $\mathcal{M}$.

Proposition 3.1. *(Law of large numbers) Let $X_1,\ldots,X_n \overset{iid}{\sim} P$ with Karcher mean μ, $n=2^J$ for some $J>0$, and such that the distribution P defined on $\mathcal{M}$ has finite second moment $\int \delta(Y,X)^2\; dP(X)<\infty$ for all $Y\in\mathcal{M}$. Then,*

$$\mu_n(X_1,\ldots,X_n) \;\overset{P}{\to}\; \mu, \qquad \text{as } n\to\infty$$

where the convergence holds with respect to the Riemannian distance, i.e. for every $\epsilon>0$, $Pr(\delta(\mu_n,\mu)>\epsilon)\to 0$.

From the proposition above, it is clear that if the Euclidean mean $\boldsymbol{E}[X_\ell]=f$ and the Karcher mean $\mathbb{E}[X_\ell]=\mu$ do not coincide, the repeated midpoint functional is not a consistent estimator of f, the quantity of interest. By defining the notion of bias on the manifold as in [24], the repeated midpoint functional of a locally averaged or multitaper spectral estimate is seen to be asymptotically biased with respect to the spectrum f.

Definition 3.1. Given an estimator $\hat{\mu}$ of $\mu \in \mathcal{M}$, define the bias $b(\hat{\mu}, \mu) \in \mathcal{T}_\mu(\mathcal{M})$ of $\hat{\mu}$ as,

$$b(\hat{\mu}, \mu) \quad = \quad \boldsymbol{E}[\mathrm{Log}_\mu(\hat{\mu})]$$

where $\boldsymbol{E}[\cdot]$ is the (ordinary) Euclidean expectation in the vector space $\mathcal{T}_\mu(\mathcal{M}) \simeq \mathcal{H}$.

Note that in the context of a Euclidean space, the exponential and logarithmic maps reduce to ordinary matrix addition and subtraction, in which case the above definition simplifies to the usual vector space definition of the bias.

Theorem 3.2. *(Bias-correction) Let* $X \sim W_d^c(B, B^{-1}f)$ *and* $c(d, B) = -\log(B) + \frac{1}{d}\sum_{i=1}^{d} \psi(B - (d-i))$*, with* $\psi(\cdot)$ *the digamma function, then the bias according to Definition 3.1 of* X *with respect to* f *is given by,*

$$b(X, f) \;=\; \boldsymbol{E}[\mathrm{Log}_f(X)] \;=\; c(d, B) \cdot f$$

If we rescale $(\widetilde{X}_\ell)_{\ell=1,\ldots,n} := (e^{-c(d,B)} X_\ell)_{\ell=1,\ldots,n}$*, where* $X_1, \ldots, X_n \overset{iid}{\sim} W_d^c(B, B^{-1}f)$*, with* $n = 2^J$ *for some* $J > 0$*, then:*

$$\mu_n(\widetilde{X}_1, \ldots, \widetilde{X}_n) \quad \overset{P}{\to} f, \qquad \text{as } n \to \infty$$

where the convergence in probability holds with respect to the Riemannian distance.

Remark Note that if $d = B = 1$, the bias-correction simplifies to multiplication by the scalar $\exp(-c(d, B)) = \exp(-\psi(1))$. This corresponds to the asymptotic bias-correction, equal to the exponential of the Euler-Mascheroni constant, typically applied when smoothing the ordinary log-periodogram in the context of a univariate time series, see e.g. [27]

3.2 Properties of wavelet coefficients

As noted before, the periodograms $I_n(\omega_\ell)$, or the pre-smoothed periodograms $\hat{f}_n(\omega_\ell)$ based on either local averaging over frequency or multitaper spectral estimation, are asymptotically independent complex Wishart matrices. The wavelet coefficients $(D_{j,k})_{j,k}$ obtained from the MI wavelet transform of a sequence of independent complex Wishart matrices display several appealing properties. Below, we write P_f for the probability distribution corresponding to a bias-corrected complex Wishart distribution $e^{-(d,B)} W_d^c(B, B^{-1}f)$ as in Theorem 3.2, with $B \geq d$ to ensure positive-definiteness of the random variable. In general, P_f is a distribution on the manifold $\mathcal{M}$ of a random variable $X = f^{1/2} * W$, where W is a $d \times d$-dimensional Hermitian PD complex Wishart matrix, with B degrees of freedom, not depending on f, and with Karcher mean equal to the identity matrix I_d. Note that the latter directly implies that $f^{1/2} * W$ has Karcher mean equal to f.

Proposition 3.3. *(Trace properties) Let $X_\ell \sim P_{f_\ell}$, for $\ell = 1, \ldots, n$, be independently distributed, with $n = 2^J$ for some $J > 0$, such that $X_\ell \in \mathcal{M}$ has Karcher mean f_ℓ. For each scale-location (j,k), the wavelet coefficients obtained from the MI wavelet transform, with refinement order $N = 2D+1$ where $D \in \mathbb{N}$, satisfy:*

$$Tr(D^X_{j,k}) \quad = \quad Tr(D^f_{j,k}) + Tr(D^W_{j,k})$$

where $D^X_{j,k}$ is the random wavelet coefficient based on the sequence $(X_\ell)_{\ell=1}^n$, $D^f_{j,k}$ is the deterministic wavelet coefficient based on the sequence of Karcher means $(f_\ell)_{\ell=1}^n$, and $D^W_{j,k}$ is the random wavelet coefficient based on a sequence of i.i.d. Wishart matrices $(W_\ell)_{\ell=1}^n$, with Karcher mean equal to the identity, independent of $(f_\ell)_{\ell=1}^n$.
Moreover,

$$\boldsymbol{E}[\,Tr(D^X_{j,k})] \quad = \quad Tr(D^f_{j,k})$$

and,

$$Var(\,Tr(D^X_{j,k})) \quad = \quad \frac{1}{2^{J-j}} \left(\sum_{-D \le \ell \le D} K_\ell^2 \right) \left(\sum_{i=1}^{d} \psi'(B-(d-i)) \right)$$

where $\psi'(\cdot)$ is the trigamma function, and $(K_\ell)_\ell$ are kernel weights equivalent to the weights in the ordinary average-interpolation scheme with refinement order N as in [9]. In particular, $Var(\,Tr(D^X_{j,\cdot})) = \frac{1}{2}\,Var(\,Tr(D^X_{j+1,\cdot}))$, and whenever $Tr(D^f_{j,k})$ vanishes, e.g. when $(f_\ell)_\ell$ is a discretized geodesic curve, $\boldsymbol{E}[\,Tr(D^X_{j,k})] = 0$.

Corollary 3.4. *(Centered noise) With the same notation as in Proposition 3.3, the random wavelet coefficients $D^W_{j,k}$ based on a sequence of i.i.d. Wishart matrices $(W_\ell)_{\ell=1}^n$, with identity Karcher mean, satisfy:*

$$\boldsymbol{E}[D^W_{j,k}] \quad = \quad \mathbf{0}_{d\times d}$$

where $\boldsymbol{E}[\cdot]$ denotes the Euclidean expectation.

Proposition 3.5. *(Moment stabilization) With the same notation as in Proposition 3.3, suppose that $(f_\ell)_{\ell=1}^n$ is locally constant for $\ell \in \{2^{J-j}(k-D)+1, \ldots, 2^{J-j}(k+D+1)\}$, where $k = 0, \ldots, 2^j - 1$ and $N = 2D+1$ with $D \in \mathbb{N}$ the order of the MI refinement scheme. The moments in terms of the Euclidean norm of the wavelet coefficients $D^X_{j,k}$ satisfy:*

$$\boldsymbol{E}\|D^X_{j,k}\|_F^p \quad = \quad \boldsymbol{E}\|D^W_{j,k}\|_F^p, \qquad \text{for any} \;\; p \in \mathbb{R}$$

In particular, the moments of $D^X_{j,k}$ do not depend on $(f_\ell)_{\ell=1}^n$. As a consequence, if the expected value $\boldsymbol{E}[D^X_{j,k}] = \mathbf{0}_{d\times d}$ vanishes, then the variance $Var(D^X_{j,k}) = \boldsymbol{E}\|D^X_{j,k}\|_F^2$ is stabilized across all locations k within scale j.

3.3 Nonlinear wavelet thresholding

In order to flexibly estimate the spectrum $f(\omega_\ell)$, we consider denoising of an initial bias-corrected Hermitian PD spectral estimate $\hat{f}_n(\omega_\ell)$ in the wavelet domain. In this work, we focus on simple nonlinear hard thresholding of wavelet coefficients, but other approaches, such as soft thresholding, or (Bayesian) shrinkage of wavelet coefficients, may be suitable as well. Nonlinear thresholding of wavelet coefficients allows for inhomogeneous smoothness behavior across frequency, as the wavelet coefficients have compact support in $[0, \pi]$. To be precise, the wavelet coefficient $D^X_{j,k}$ depends on the initial noisy curve $(\hat{f}_n(\omega_\ell))_\ell$ at the frequencies $\omega_\ell \in [2^{-j}(k-D)\pi, 2^{-j}(k+1+D)\pi]$, where $N = 2D+1$ is the order of the MI refinement scheme. We do not consider thresholding on the level of the entire matrix-valued coefficients $D^X_{j,k}$. Instead, we decompose the Hermitian matrices $D^X_{j,k}$ with respect to an orthonormal basis $(E_i)_{i=1,\dots,d^2}$ of the real vector space of Hermitian matrices $\mathcal{H}$, orthonormal in terms of $\langle \cdot, \cdot \rangle_F$. Nonlinear thresholding is then performed on the level of the individual components of the wavelet coefficients $d^{i,X}_{j,k} := \langle D^X_{j,k}, E_i \rangle_F \in \mathbb{R}$. This enables us to capture inhomogeneous smoothness behavior across different components of the spectral matrix, and we only have to consider thresholding of real-valued components (instead of complex- or matrix-valued coefficients). The wavelet-thresholded spectral estimator is guaranteed to be positive-definite as the inverse wavelet transform maps the sequence of thresholded wavelet coefficients to a curve on the manifold $\mathcal{M}$. For computational simplicity, we consider one single hard threshold $\lambda \in \mathbb{R}_+$ applied to all components of the wavelet coefficients $(d^{i,X}_{j,k})_{j,k,i}$. This is partially justified by the observation that a zero wavelet coefficient $D^X_{j,k}$ is approximately unitarily invariant, thus permuting the components $(d^{i,X}_{j,k})_i$ does not affect their joint distribution. Also, simulation results based on multiple thresholds $(\lambda_1, \dots, \lambda_{d^2})$ do not show a significant increase in performance. Note, however, that from a theoretical point of view we are not restricted to the use of a single threshold in the different basis directions $i = 1, \dots, d^2$. The nonlinear wavelet thresholding procedure is described step by step in Algorithm 1 below.

3.3.1 Permutation-equivariance

In general, it is desirable that a reordering of the d components of the d-dimensional time series $\vec{Y}(t) = (Y_1(t), \dots, Y_d(t))'$ does not influence the computed spectral estimator $\hat{f}(\omega)$ apart from permuting the estimated matrix elements. If the opposite is true, it is not clear which ordering to consider for estimation. To be precise, suppose we observe a permutation $\pi(1, \dots, d)$ of the ordering of the components of the time series, then the spectral matrix of the permuted time series is expressed as $f_\pi(\omega) = U_\pi * f(\omega)$, where U_π is the permutation matrix corresponding to the permutation $\pi(1, \dots, d)$. We wish the spectral estimator to satisfy this property as well, i.e. $\hat{f}_\pi(\omega_\ell) = U_\pi * \hat{f}(\omega_\ell)$ for any permutation matrix U_π, so that the spectral estimator is invariant up to a permutation of matrix elements of $\hat{f}(\omega_\ell)$.

Algorithm 1: (Nonlinear wavelet thresholding procedure)

Input : Bias-corrected HPD periodogram $\boldsymbol{X} = (\hat{f}_{\text{per}}(\omega_\ell))_\ell$ and thresholds $(\lambda_i)_i$
Output: Wavelet-denoised HPD spectral estimate $\hat{\boldsymbol{f}} = (\hat{f}_\lambda(\omega_\ell))_\ell$

1 Compute the wavelet transform of $\boldsymbol{X}$, returning coarse-scale midpoints $(M^X_{1,0}, M^X_{1,1})$ and the pyramid of wavelet coefficients $(D^X_{j,k})_{j,k}$.
2 Decompose the wavelet coefficients $d^{X,i}_{j,k} = \langle D^X_{j,k}, E_i \rangle_F \in \mathbb{R}$ with respect to an orthonormal basis $(E_i)_i$ of the real vector space $\mathcal{H}$
3 Normalize the variance of the components $(d^{X,i}_{j,k})_{i,j,k}$ across wavelet scales by one of the methods in Section 3.3.2, denoting the rescaled components by $(\tilde{d}^{X,i}_{j,k})_{i,j,k}$.
4 Threshold the rescaled components $d^{\hat{f},i}_{j,k} = d^{X,i}_{j,k} \mathbf{1}\{|\tilde{d}^{X,i}_{j,k}| > \lambda_i\}$ for each i, j, k.
5 Recompose the thresholded wavelet coefficients $D^{\hat{f}}_{j,k} = \sum_{i=1}^{d^2} d^{\hat{f},i}_{j,k} E_i$ for each j, k.
6 Compute the inverse wavelet transform of the thresholded wavelet coefficients $(D^{\hat{f}}_{j,k})_{j,k}$ combined with the coarse-scale midpoints $(M^X_{1,0}, M^X_{1,1})$. This returns the wavelet-thresholded spectral estimate $\hat{\boldsymbol{f}}$.

Unfortunately, the spectral estimation methods based on smoothing the Cholesky decomposition of an initial noisy spectral estimator ([7], [23], or [17]) are not necessarily equivariant under a permutation of the components of the time series. This is due to the fact that the Cholesky matrix is not permutation-equivariant, i.e. $\text{Chol}(U_\pi * f(\omega)) \neq U_\pi * \text{Chol}(f(\omega))$ for a non-trivial permutation matrix U_π, and as a consequence the Cholesky-smoothed spectral estimator also fails to satisfy the permutation-equivariance property. The proposition below states that the equivariance property does hold true for the nonlinear hard wavelet-thresholded spectral estimator.

Proposition 3.6. *(Permutation-equivariance) Let U_π be a $d \times d$-dimensional permutation matrix corresponding to a permutation $\pi(1, \ldots, d)$ of the components of the time series. The nonlinear hard wavelet-thresholded spectral estimator $\hat{f}_{\sigma(\vec{\lambda}),\pi}(\omega_\ell)$ under the permuted ordering $\pi(1, \ldots, d)$ of the time series, with permuted threshold vector $\sigma(\vec{\lambda}) = \sigma(\lambda_1, \ldots, \lambda_{d^2}) \in \mathbb{R}^{d^2}_+$ satisfies $\hat{f}_{\sigma(\vec{\lambda}),\pi}(\omega_\ell) = U_\pi * \hat{f}_{\vec{\lambda}}(\omega_\ell)$ for each $\omega_\ell \in (0, \pi]$, where $\hat{f}_{\vec{\lambda}}(\omega_\ell)$ is the wavelet-thresholded spectral estimator under the non-permuted ordering of the time series, with threshold vector $\vec{\lambda} = (\lambda_1, \ldots, \lambda_{d^2})$.*

3.3.2 Variance normalization

An important difference regarding the introduced manifold wavelet transform compared to most traditional wavelet-thresholding procedures in a Euclidean space, is that the variances of the (components of) wavelet coefficients are not homogeneous across scales. Note that we also do not include a scaling factor for the wavelet coefficients in contrast to [22]. If

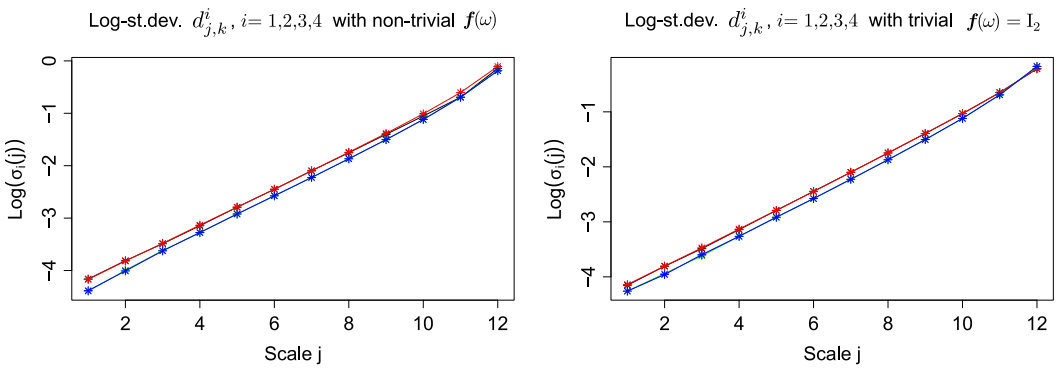

Figure 3: Log standard-deviations of components $d^{i,X}_{j,k}$, $i = 1, 2, 3, 4$, of the matrix-valued wavelet coefficients across scales, based on a non-trivial spectrum $f(\omega)$ on the left, and a trivial spectrum $f(\omega) = \mathrm{I}_2$ on the right.

we use a scale-dependent threshold λ_j to threshold the wavelet coefficients at wavelet scale j this is not a problem. However, if we wish to use a single threshold λ to threshold coefficients at each scale j, the variances of the wavelet coefficients should be homogeneous across scales. By Proposition 3.3, the variance of the trace of a noisy wavelet coefficient $\mathrm{Var}(\mathrm{Tr}(D^X_{j,k}))$ decreases by a factor $1/2$ per scale, as typically the case for wavelet coefficients in a Euclidean space. For the variance of individual components $\mathrm{Var}(d^{i,X}_{j,k})$ this is no longer exactly true due to the non-zero curvature of the Riemannian manifold $\mathcal{M}$. To illustrate, for two random variables on the manifold $X_1, X_2 \overset{\text{iid}}{\sim} P_f$ with Karcher mean $f \in \mathcal{M}$, instead of an equality, we find only the inequality $\boldsymbol{E}[\delta(\mathrm{Mid}(X_1, X_2), f)^2] \leq \frac{1}{2}\boldsymbol{E}[\delta(X_1, f)^2]$.

One straightforward approach to normalize variances across wavelet scales is to simulate many initial positive-definite spectral estimates with a trivial underlying spectrum, e.g. $f(\omega) = \mathrm{I}_d$, and use the simulated variances as a benchmark to normalize the variances of the wavelet coefficients with non-trivial underlying spectrum that we are trying to estimate. This is illustrated in Figure 3, where we compute the standard deviations of components of wavelet coefficients (averaged within scale) for simulated pre-smoothed periodograms of a 2-dimensional time series (1000 instances), with non-trivial dummy spectrum $f(\omega)$ on the left, and trivial spectrum $f(\omega) = \mathrm{I}_2$ on the right.
This approach works well when the number of wavelet scales J is relatively small, but is computationally expensive when J becomes increasingly large. As an alternative, we consider simple weighted linear regression to estimate the log-variances across scales, which still increase approximately linearly per scale. The linear regression curves are fitted using weighted least squares estimation with a $J \times J$-dimensional diagonal weight matrix $W = \mathrm{diag}(\exp(\alpha), \exp(2\alpha), \ldots, \exp(J\alpha))$. In this way, the weight matrix attributes larger weights to increasingly fine wavelet scales. The reasoning is that for relatively sparse signals in the wavelet domain, finer wavelet scales contain primarily zero wavelet coefficients, and

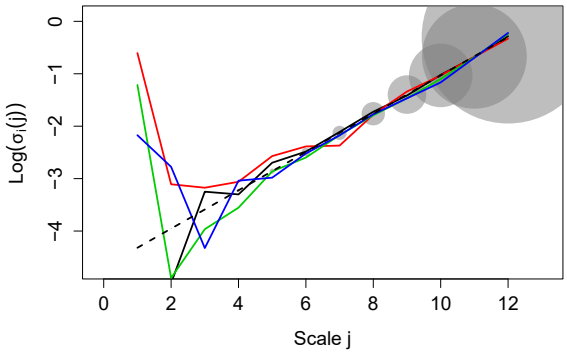

Figure 4: Sample standard deviations (colored curves) and estimated regression curve (dashed line), with the radii of the circles equal to the relative weights attributed to each scale ($\alpha = 0.5$).

thus give more reliable estimates of the variances of the coefficients. In Figure 4, the colored curves show the sample standard deviations of the components $(d_{j,k}^{i,X})_{i=1,2,3,4}$ of the wavelet coefficients (averaged within scale) for a simulated pre-smoothed periodogram of a 2-dimensional time series, with non-trivial dummy spectrum $f(\omega)$ as in Figure 3. The dashed line shows the estimated regression curve, which is used to normalize the variances of the components across scales. Without prior knowledge of the sparsity of the signal, a choice of the weighting parameter $\alpha \in [0.5, 1)$ seems reasonable in most settings.

3.3.3 Threshold selection

After normalization of the variances of the components of the wavelet coefficients, we pool together all the components $(d_{j,k}^{i,X})_{j,k,i}$ and apply a single hard threshold $\lambda \in \mathbb{R}_+$ to their absolute values. Below, we consider threshold selection based on two-fold cross-validation as proposed in [19] due to its good empirical performance, but other threshold selection methods may be appropriate as well. Note that the noise distribution of the wavelet coefficients does not exactly follow a Gaussian distribution, therefore we have to be cautious when applying thresholding procedures based on Gaussian noise assumptions.

Suppose that $(\hat{f}_n(\omega_\ell))_{\ell=1,\dots,n}$ is an initial noisy Hermitian PD spectral estimator, with $n = 2^J$ for some $J > 0$. The threshold selection proceeds as follows:

1. Remove all the odd-indexed observations $\hat{f}_n(\omega_{2i-1})$ and construct the wavelet-thresholded spectral estimator $\hat{f}_\lambda(\omega_{2i})$ for $i = 1, \dots, n/2$, with threshold $\lambda \in \mathbb{R}_+$ based only on the even-indexed observations. Analogously, by leaving out the even-indexed observations $\hat{f}_n(\omega_{2i})$, construct $\hat{f}_\lambda(\omega_{2i-1})$ for $i = 1, \dots, n/2$ based only on the odd-indexed observations.

2. Construct interpolated versions of the even-indexed $(\hat{f}_\lambda(\omega_{2i}))_i$ and odd-indexed $(\hat{f}_\lambda(\omega_{2i-1}))_i$

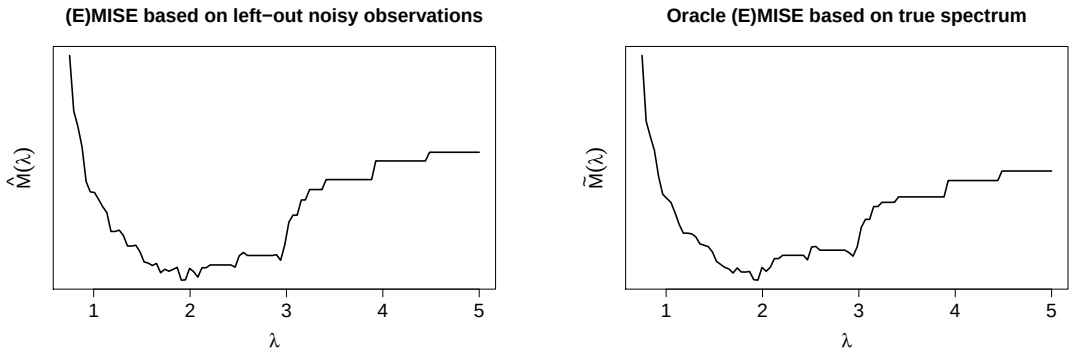

Figure 5: Cross-validation estimated MISE $\widehat{M}(\lambda)$ on the left, and the *oracle* estimated MISE $\widetilde{M}(\lambda)$ on the right.

estimates through:

$$\begin{aligned} \tilde{f}_\lambda(\omega_{2i-1}) &= \text{Mid}\left\{\hat{f}_\lambda(\omega_{2i-2}), \hat{f}_\lambda(\omega_{2i})\right\}, \qquad \text{for } i = 2, \ldots, n/2 \\ \tilde{f}_\lambda(\omega_{2i}) &= \text{Mid}\left\{\hat{f}_\lambda(\omega_{2i-1}), \hat{f}_\lambda(\omega_{2i+1})\right\}, \qquad \text{for } i = 1, \ldots, n/2-1 \end{aligned}$$

where we set $\tilde{f}_\lambda(\omega_1) = \hat{f}_\lambda(\omega_2)$ and $\tilde{f}_\lambda(\omega_n) = \hat{f}_\lambda(\omega_{n-1})$.

3. Estimate the mean integrated squared error (MISE) between the interpolated spectral estimates and the left-out observations:

$$\widehat{M}(\lambda) = \sum_{i=1}^{n/2} \left[\delta(\tilde{f}_\lambda(\omega_{2i-1}), \hat{f}_n(\omega_{2i-1})) + \delta(\tilde{f}_\lambda(\omega_{2i}), \hat{f}_n(\omega_{2i}))\right]$$

based on the Riemannian distance function $\delta(\cdot,\cdot)$ in eq.(2.1).

4. Minimize $\widehat{M}(\lambda)$ with respect to the threshold λ via a simple golden section search, similar to [19].

In Figure 5 on the left, we display $\widehat{M}(\lambda)$ for different values of λ, where the data is obtained from a simulated 2-dimensional time series, with a non-trivial underlying dummy spectrum $f(\omega)$. In this example, we fix the primary thresholding scale at $j_0 = 2$, but a more informed choice can be obtained by also incorporating the primary thresholding scale in the cross-validation procedure. Furthermore, in order to remove isolated noise singularities, we applied a simple post-processing step imposing a connected top-down tree-structure on the pyramid of non-zero wavelet coefficients, see e.g [13, Chapter 5]. In short, whenever we encounter a component $\hat{d}^{i,X}_{j,k}$ that has been set to zero, we automatically set to zero all its descendants $\hat{d}^{i,X}_{j+1,2k}$, $\hat{d}^{i,X}_{j+1,2k+1}$, etc. In Figure 5 on the right, we display the *oracle* estimated MISE computed as $\widetilde{M}(\lambda) = \sum_{i=1}^{n} \delta(\tilde{f}_\lambda(\omega_i), f(\omega_i))$, based on the true underlying spectrum $(f(\omega_i))_i$. We observe that the minima for both error functions are located at approximately the same values of λ.

4 Clustering of spectral matrices

As an additional application of the proposed wavelet methodology, we outline a computationally fast approach to clustering of multivariate spectral matrices, i.e. clustering of multivariate time series in the frequency domain, based on their representations in the wavelet domain. The motivating principle is that relatively *smooth* spectral curves on the manifold $\mathcal{M}$ are summarized by few coarse-scale wavelet coefficients, thereby allowing for fast clustering in the wavelet domain based on few high-energy features. This approach is benchmarked in terms of computation time against direct clustering of spectral curves in the frequency domain in Section 5.1.

Consider a d-dimensional mean-zero stationary observed time series $(\vec{Y}^s(1), \ldots, \vec{Y}^s(T))$, with spectral matrix $f^s(\omega)$ for subject $s = 1, \ldots, S$. Let $\hat{f}_n^s(\omega_\ell)$ be an initial noisy Hermitian PD spectral estimator for subject s at Fourier frequency $\omega_\ell \in (0, \pi]$, with $\ell = 1, \ldots, n$ and $n = T/2 = 2^J$ for some $J > 0$. We assume that the number of clusters K is specified in advance, for informed choice of K we refer to e.g. [1, Chapter 4]. The S subjects are assigned to the K clusters with different probabilities through a two-step fuzzy c-means algorithm in the wavelet domain:

1. For each $s = 1, \ldots, S$, compute the forward MI wavelet transform of $(\hat{f}_n^s(\omega_\ell))_\ell$ resulting in the coarsest-scale midpoints $(M_{1,0}^s, M_{1,1}^s)$ and the pyramid of wavelet coefficients $(D_{j,k}^s)_{j,k}$ for $j = 1, \ldots, J-1$ and $k = 0, \ldots, 2^j - 1$. Normalize the variance of the wavelet coefficients across scales and threshold the components as in Algorithm 1 based on the hard threshold λ_s, where λ_s is selected by e.g. cross-validation.

2. Apply a fuzzy c-means algorithm to the coarsest scale midpoints based on the Riemannian distance function, where each subject s has two features $(M_{1,0}^s, M_{1,1}^s)$.

3. Initialize cluster centers based on the cluster assignments found in the previous step, and apply a weighted fuzzy c-means algorithm to the non-zero thresholded wavelet coefficients at scales $1, \ldots, j_{\max}$ based on the Euclidean distance.

The geometric fuzzy c-means algorithm based on the Riemannian distance function in step 2., and the weighted fuzzy c-means algorithm in step 3. are discussed in more detail below. First, we point out that the cluster assignments are invariant under permutation of the components of the time series in the same sense as in Section 3.3.1.

Proposition 4.1. *(Permutation-invariance) If $\pi(1, \ldots, d)$ is a permutation of the ordering of the components $1, \ldots, d$ of the d-dimensional subject-specific time series identical for each subject $s = 1, \ldots, S$. Then the fuzzy cluster assignments under the permuted ordering $\pi(1, \ldots, d)$ of the time series traces are equivalent to the fuzzy cluster assignments under the original non-permuted ordering of the time series traces.*

Geometric fuzzy c-means in step 2. In step 2. of the clustering procedure, we consider minimization of a *within-cluster sum of squared distances* (WCSSD) functional with fuzziness parameter (weighting exponent) $m \in (1, \infty)$ given by:

$$J_M(U) \quad = \quad \sum_{k=1}^{K} \sum_{s=1}^{S} \sum_{i=0}^{1} (U_{sk})^m \delta(M_{1,i}^s, \overline{M}_{1,i}^k)^2 \tag{4.1}$$

which we wish to minimize with respect to the fuzzy partition matrix $U \in \mathcal{U}_{fc}$, where,

$$\mathcal{U}_{fc} \quad = \quad \left\{ U \in [0,1]^{S \times K} \;\middle|\; \forall s,\ \sum_{k=1}^{K} U_{sk} = 1,\ \text{and } \forall k,\ 0 < \sum_{s=1}^{S} U_{sk} < K \right\} \tag{4.2}$$

The cluster centers $\overline{M}_{1,i}^k$ are empirical *weighted* Karcher means of the observations $(M_{1,i}^s)_s$ based on the membership probabilities U_{sk} with respect to the cluster k. To calculate an empirical weighted Karcher mean from observations $(M_s)_s$ with weights $(w_s)_s$, satisfying $\sum_s w_s = 1$, we adopt a generalized version of the gradient descent algorithm described in [20], computing the limiting value of:

$$\overline{M}_{(t+1)} \quad = \quad \mathrm{Exp}_{\overline{M}_{(t)}} \left(\sum_{s=1}^{S} w_s \mathrm{Log}_{\overline{M}_{(t)}} (M_s) \right) \tag{4.3}$$

Note that in the context of Euclidean space, since the exponential and logarithmic maps reduce to ordinary matrix addition and subtraction, the above formula simplifies to the weighted mean $\overline{M}_{(t+1)} = \sum_s w_s M_s$, which converges in a single iteration. As a computationally less expensive alternative, it is also possible to consider an approximate version of the empirical weighted Karcher mean, which is computed recursively as:

$$\begin{cases} \overline{M}_{(1)} \;=\; M_1 \\ \overline{M}_{(s+1)} \;=\; \gamma \left(\overline{M}_{(s)}, M_{s+1}, \frac{w_{s+1}}{\sum_{i=1}^{s+1} w_i} \right) \quad \text{for } s = 1, \ldots, S-1 \end{cases} \tag{4.4}$$

where $\gamma(\cdot)$ is the connecting geodesic on $\mathcal{M}$ as in eq.(2.2). If the weights w_s are equal for each $s = 1, \ldots, S$, then the above expression reduces to the approximate empirical (unweighted) Karcher mean considered in e.g. [12].

The objective functional in eq.(4.1) is minimized by a fuzzy c-means algorithm based on the Riemannian distance function, the full details can be found in the appendix. In applying a (fuzzy) c-means algorithm based on the Riemannian distance function, it is important that the cluster center updates are based on empirical Karcher means of the manifold-valued data, instead of e.g. empirical Euclidean means. Besides the fact that the Karcher mean gives a more natural measure of centrality for manifold-valued data, this is important because the empirical Karcher mean is the least squares estimator with respect to the Riemannian distance function. This is also observed from the population Karcher expectation in eq.(3.1). In this way, we ensure that both the assignment step and the update step

in the (fuzzy) c-means algorithm minimize the WCSSD objective in eq.(4.1). To further illustrate this, consider the c-means algorithm with fuzziness parameter $m \to 1$, in which case the fuzzy c-means algorithm reduces to a non-fuzzy c-means algorithm. Since both the assignment step and the update step optimize the WCSSD objective, and in the non-fuzzy situation there exist only a finite number of cluster partitionings, the c-means algorithm is guaranteed to converge to a (local) optimum. If on the other hand, the cluster center updates are based on empirical Euclidean means, convergence of the algorithm can no longer be guaranteed. For general m, proofs of (local) convergence of the fuzzy c-means algorithm becomes more tedious and we refer the interested reader to [1, Chapter 3].

Weighted fuzzy c-means in step 3. In step 3. of the clustering procedure, we consider the WCSSD functional with fuzziness parameter $m \in (1, \infty)$ given by:

$$J_D(U) \quad = \quad \sum_{k=1}^{K} \sum_{s=1}^{S} \sum_{j=1}^{j_{\max}} \sum_{i=0}^{2^j-1} w_{jsk} (U_{sk})^m \| D_{j,i}^s - \overline{D}_{j,i}^k \|_F^2 \tag{4.5}$$

which is again minimized with respect to the fuzzy partition matrix $U \in \mathcal{U}_{fc}$. Here, the cluster centers $\overline{D}_{j,i}^k$ are Euclidean weighted means of $(D_{j,i}^s)_s$ based on the weights $(U_{sk})_s$, with $\sum_s U_{sk} = 1$. This is appropriate as the wavelet coefficients are elements of the real vector space $\mathcal{H}$. Note that we incorporate additional weights w_{jsk}, which are given by,

$$w_{jsk} \quad = \quad 2^{(j_{\max}-j)} \frac{1 - \exp(-\tau \mathrm{dist}_{sk}^0)}{1 + \exp(-\tau \mathrm{dist}_{sk}^0)}$$

Here $\mathrm{dist}_{sk}^0 := \sum_{i=0}^{1} \delta(M_{1,i}^s, \overline{M}_{1,i}^k)^2$ is the distance between the midpoint vector $(M_{1,1}^s, M_{1,2}^s)$ for subject s and the cluster center $(\overline{M}_{1,1}^k, \overline{M}_{1,2}^k)$ for cluster k found at the final iteration of the fuzzy c-means algorithm in step 2. Through the weights w_{jsk}, we incorporate prior information on the previously obtained cluster assignments. To illustrate heuristically, consider obtaining a high probability cluster assignment of subject s to cluster k after execution of the fuzzy c-means algorithm in step 2. This implies that dist_{sk}^0 is relatively small, and as a consequence the weight w_{jsk} is also small. In minimizing the functional in eq.(4.5), the distances corresponding to old high probability cluster assignments are downweighted and therefore preferred when executing the weighted fuzzy c-means algorithm.
The tuning parameter $\tau > 0$ allows to control the weight attributed to the previously obtained cluster assignments, see also [25], where the authors discuss including prior information in a weighted c-means clustering algorithm in a different context. Furthermore, w_{jsk} includes a scaling factor $2^{(j_{\max}-j)}$ for features at wavelet scale j. This scaling factor assigns increased importance (i.e. higher weight) to features located at coarse wavelet scales, describing global or average structural behavior of the spectral curves. On the other hand, we assign lower weights to features located at finer wavelet scales, which primarily describe detail or local structural behavior of the spectral curves. By adjusting the weights, one can

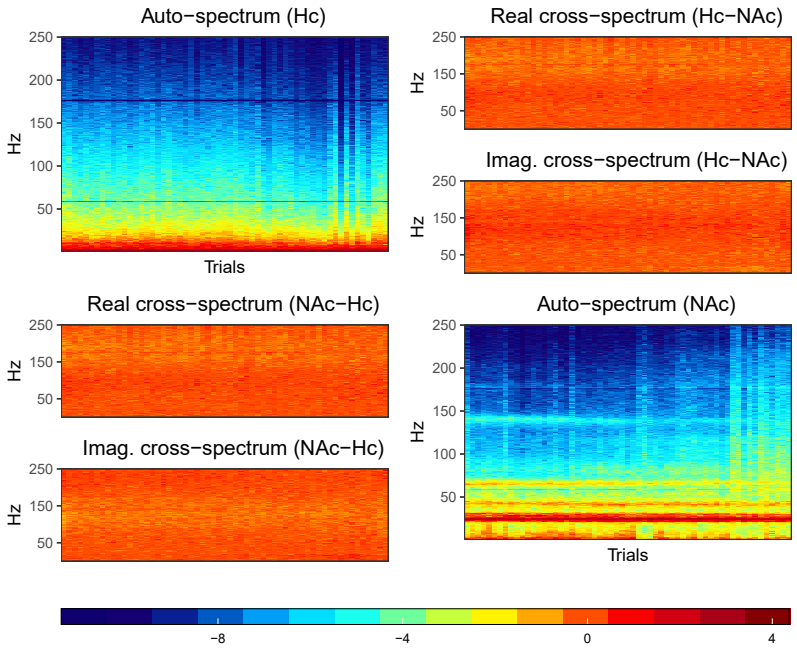

Figure 6: Matrix-logarithms of block-averaged periodograms across LFP time series trials over the course of the experiment.

focus on e.g. the spectral behavior in a specific frequency band, or highly localized spectral behavior (peaks or troughs). The finest clustering scale is fixed at some scale $j_{\max} \leq J-1$, such that at finer wavelet scales $j > j_{\max}$ most thresholded wavelet coefficients are equal to zero. Note that, as an uninformed choice, we can always set $j_{\max} = J-1$ at the cost of increased computational effort. The objective functional in eq.(4.5) is minimized by an (ordinary) fuzzy c-means algorithm based on the Euclidean distance between matrices, the details of which are found in the appendix.

5 Data examples

To demonstrate the proposed wavelet denoising and clustering methology, we analyze a brain signal dataset consisting of local field potential (LFP) time series trials recorded over the course of an associative learning experiment, see [11], [10], or [5] for a more detailed description. The goal of the analysis is to study evolving spectral characteristics of the time series trials over the course of the experiment. In [10], the authors captured the evolving spectral behavior of LFP time series trials by a specific time-evolution model across trials. To illustrate our methodology, we consider the evolving spectral behavior from another perspective by looking for common structure in the spectral matrices across trials based on cluster analysis of the estimated trial-specific spectral matrices. After preprocessing of the LFP time series data, there remain a total of 590 trial-specific approximately stationary

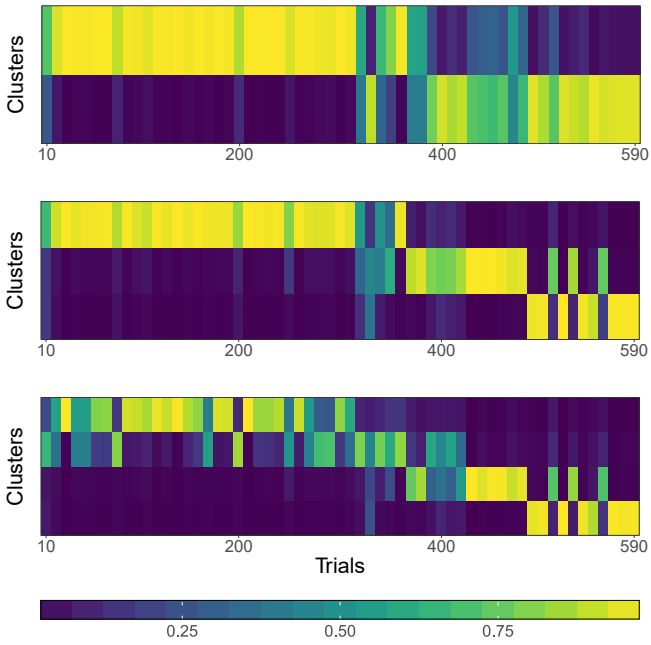

Figure 7: Probabilistic membership assignments for $K = 2, 3, 4$ clusters (top to bottom) of the LFP time series trials over the course of the experiment.

2-dimensional time series traces of length 2048 sampled at 1000 Hz, thus roughly corresponding to 2 seconds of data. The two components of the time series traces, correspond to LFP measurements in the hippocampus (Hc) and nucleus accumbens (NAc) regions of the brain. In Figure 4 we display the matrix logarithms of the initial pre-smoothed periodogram matrices up to 250 Hz, where we averaged over blocks of 10 adjacent trial-specific periodograms in order to ensure positive-definiteness and improve visibility in the image, thereby considering 59 block-averaged periodogram matrices in the analysis.

Figure 7 displays the fuzzy cluster assignments according to the wavelet-based clustering procedure for several different numbers of clusters K, with parameters ($m = 2$, $\tau = 0.5$). Focusing on the membership assignments for $K = 3$ clusters, we clearly distinguish three different phases of spectral behavior over the course of the experiment: (i) an initial phase until approximately half of the experiment, (ii) a transition phase, and (iii) a final phase at the end of the experiment. Computing the empirical weighted Karcher means of the wavelet-thresholded spectral estimates $(\hat{f}^s_\lambda(\omega))_s$, with weights based on the cluster assignment probabilities $(U_{sk})_s$, we find the representative spectral estimates for each respective cluster. This *average* spectral behavior in each of the three different phases is displayed in Figure 8. In Figure 9 we show the coherence matrices corresponding to the representative estimated spectral matrices in Figure 8. Here, the non-squared coherence at frequency ω between two components x and y of the time series is given by $c_{xy}(\omega) = |f_{xy}(\omega)|/\sqrt{f_{xx}(\omega)f_{yy}(\omega)}$,

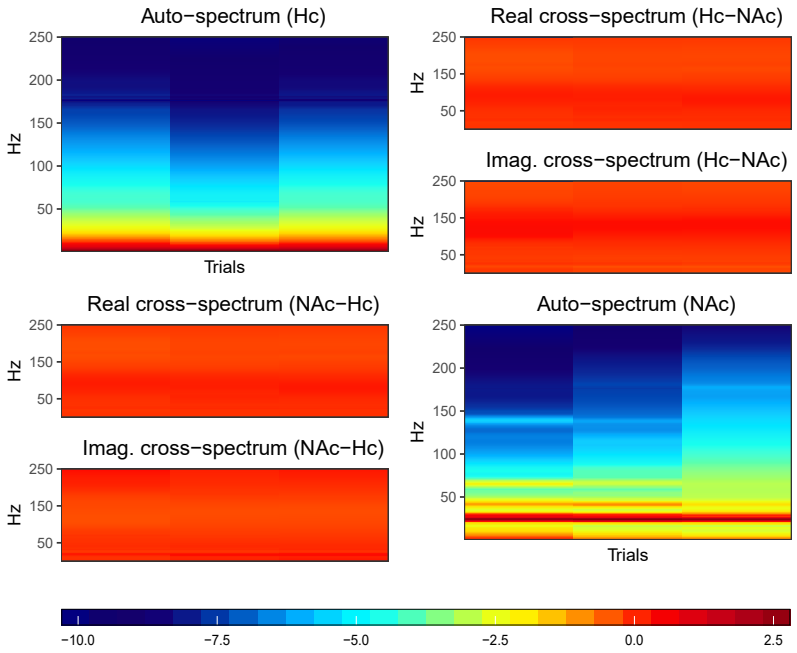

Figure 8: Matrix logarithms of representative spectral estimates for $K = 3$ clusters of the LFP time series trials.

where $f_{xy}(\omega)$ denotes the cross-spectral density between components x and y, and $f_{xx}(\omega)$ and $f_{yy}(\omega)$ denote the auto-spectral densities of the components x and y respectively. Note that the coherence between the Hc- and NAc-regions at low frequencies (up to 50 Hz) increases across the different phases in the experiment. This agrees with the results in [10], where the evolving (nonstationary) spectral behavior over the course of the experiment is investigated up to approximately 50 Hz.

5.1 Benchmarking and computation time

The computational effort and membership assignments of the wavelet-based clustering procedure are benchmarked against the alternative approach of clustering spectral curves directly in the frequency domain. The benchmark procedure entails clustering the estimated spectral curves by a fuzzy c-means algorithm based on the integrated Riemannian distance over frequency. For two spectral matrices $f(\omega)$ and $g(\omega)$, their integrated squared distance is given by:

$$\int_0^\pi \delta(f(\omega), g(\omega))^2 \, d\omega \quad \approx \quad \sum_{\ell=0}^{m} \delta(f(\omega_\ell), g(\omega_\ell))^2$$

Note that the benchmark procedure is essentially equivalent to the fuzzy c-means algorithm in step 2. of the algorithm in Section 4, but with each subject s having 2^J features $(M^s_{J,0}, \ldots, M^s_{J,2^J-1})$, instead of only two features $(M^s_{1,0}, M^s_{1,1})$.

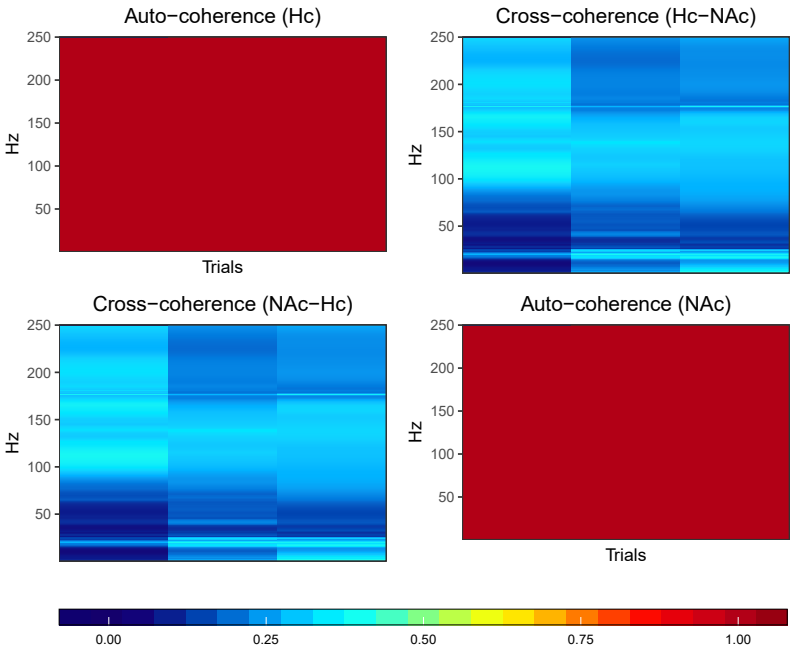

Figure 9: Representative coherence estimates for $K = 3$ clusters of the LFP time series trials.

In fact, this is a particular case of the suggested clustering methodology in [15], where the authors consider clustering multivariate time series in the frequency domain based on integrated disparity measures of the form:

$$D_H(f, g) \quad = \quad \int_0^\pi H(f(\omega)g(\omega)^{-1})\ d\omega$$

In our case, the disparity measure $H(\cdot)$ is given by,

$$H(f(\omega)g(\omega)^{-1}) \quad = \quad \|\mathrm{Log}(f(\omega)g(\omega)^{-1})\|_F^2$$

by definition of the Riemannian distance $\delta(\cdot, \cdot)$. In [15], the considered disparity measures include symmetric J-divergence and symmetric Chernoff-information divergence, which are only *quasi-distance* functions in the Euclidean space, as the triangle inequality does not hold. In contrast, the Riemannian distance is a proper distance function on the Riemannian manifold $\mathcal{M}$. Furthermore, in [15] the authors carry out c-means clustering by computing cluster center updates based on empirical Euclidean means. In the benchmark procedure above, the cluster center updates are based on empirical Karcher means of the manifold-valued data, which are more natural measures of centrality on the manifold and essential in guaranteeing (local) convergence of the c-means algorithm as argued in Section 4. Unfortunately, the empirical Karcher means –even the approximate versions in eq.(4.4)– are computationally much more expensive than their Euclidean counterparts. The fuzzy

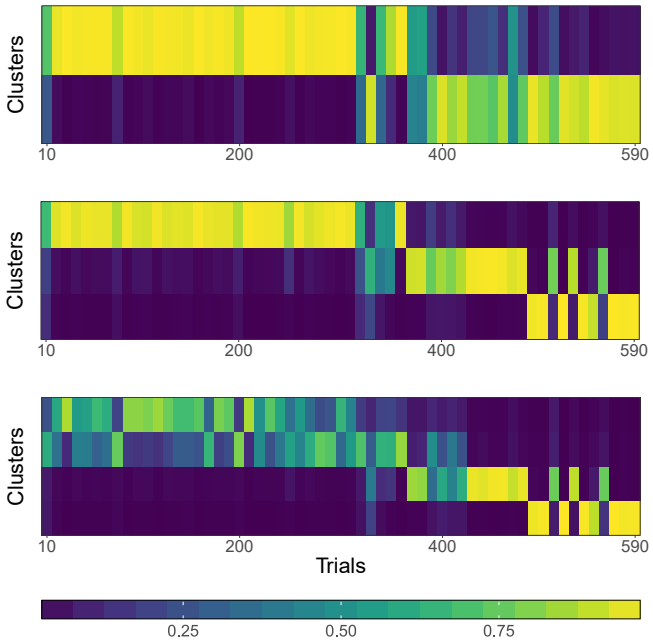

Figure 10: Probabilistic benchmark membership assignments for $K = 2, 3, 4$ clusters (top to bottom) of LFP time series trials over the course of the experiment.

cluster assignments obtained from the benchmark procedure are largely similar to the assignments obtained from the wavelet-based clustering algorithm as observed in Figure 10.

In order to measure the gain in computational speed of the wavelet-based procedure with respect to the benchmark procedure, we computed the average execution time of 10 iterations of both procedures under several different scenarios (10 iterations for both c-means algorithms in the wavelet-based procedure). Note that we chose to compare an equivalent number of iterations, instead of equivalent stopping criteria in the clustering algorithms, because the termination thresholds ϵ in both procedures are not easily comparable (one measures a total Euclidean distance, whereas the other measures a total Riemannian distance, see the appendix for the details). The maximum wavelet scale $j_{\max}$ in the wavelet-based procedure is fixed to be one of three possibilities: $j_{\max}$ is the first scale j such that either $d_j^{>0} < 0.05$, $d_j^{>0} < 0.10$, or $d_j^{>0} < 0.15$, where $d_j^{>0}$ is the proportion of non-zero components of wavelet coefficients at scale j. In the top-left image of Figure 11 we display the average computation time of the wavelet-based procedures (1000 instances) versus the benchmark procedure (100 instances) as a function of the number of clusters K, where in each instance we simulated $S = 100$ dummy wavelet-thresholded 5×5-dimensional random spectral curves of length $n = 512$. Similarly, the top right-image shows the average execution time as a function of the number of subjects S, $(K = 5, n = 512)$, and the bottom-middle image the average execution time as a function of the number of frequencies n, $(K = 5, S = 100)$. The

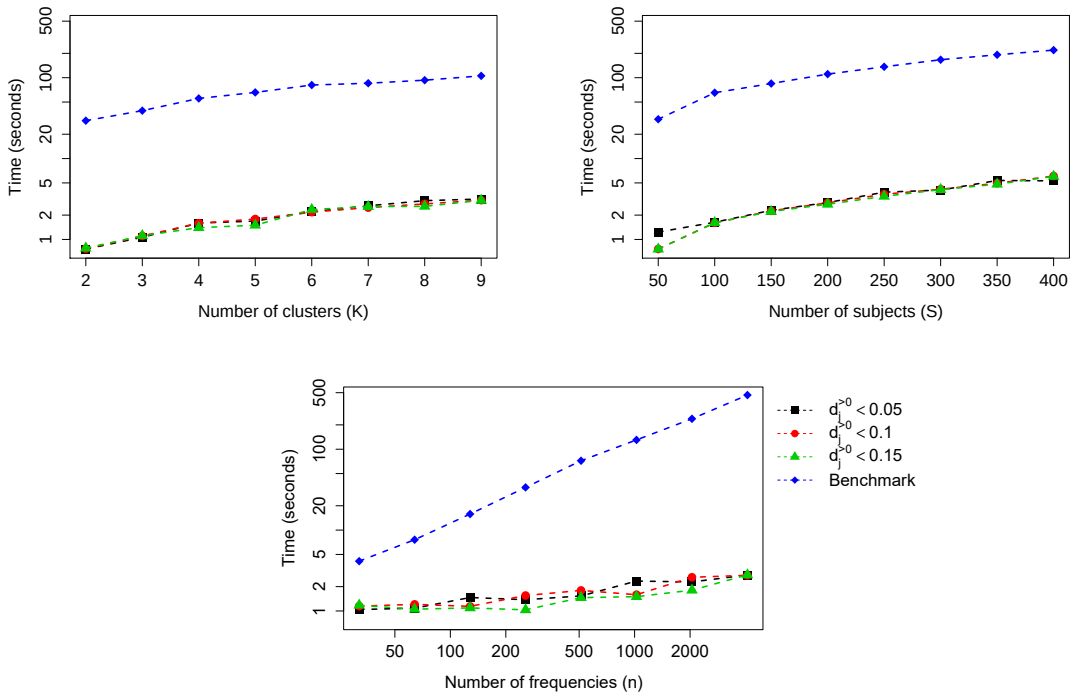

Figure 11: Average execution time of 10 iterations of the wavelet-based clustering procedure versus the benchmark clustering procedure under several different scenarios.

figures show an increase in computational speed of the wavelet-based procedure with respect to the benchmark procedure ranging between factors 20 to 250, depending on the initialization of the parameters. These results illustrate the potential gains in computational speed especially for databases consisting of a large number of time series trials sampled at high rates, for which traditional clustering procedures may become computationally very expensive. We emphasize that the reduced computation time is directly linked to the sparseness of the estimated spectral curves in the wavelet domain, with increasingly sparse representations resulting in lower computational effort for the wavelet-based clustering procedure.

6 Conclusion

In this work we developed a framework for wavelet-based spectral curve estimation and clustering on the Riemannian manifold $\mathcal{M}$ of Hermitian PD matrices. This appears to be a more natural approach than matrix-valued curve estimation of Hermitian PD matrices embedded in a Euclidean space. Although we focused only on estimation and clustering of spectral density matrices, the methodology applies to general matrix-valued curve estimation and clustering problems, where the targets are curves of symmetric or Hermitian PD

matrices. The spectral estimation approach is essentially a generalization of wavelet-based smoothing of the log-periodogram of a univariate time series to the multivariate time series setting. This is illustrated by the asymptotic manifold bias-correction, which generalizes the bias-correction for the log-periodogram in [27], or the fact that the variances of the matrix-valued wavelet coefficients are approximately stabilized within wavelet scales similar to the univariate case. The key to deriving the main results in this paper is the fact that the Riemannian manifold $\mathcal{M}$ endowed with the natural Riemannian distance function is a geodesically complete manifold without cut-locus, which, although being non-Euclidean, is still a very well-structured space. This allows for the development of useful statistical tools, such as a well-defined wavelet transform on the entire manifold, or the unique and existing expectation of a manifold-valued random variable. In addition to wavelet-based multivariate spectral estimation, we also outlined an approach to perform computationally fast clustering of multivariate spectral curves, based on their representations in the wavelet domain. Other generalizations from a univariate to a multivariate spectral analysis context – with spectral curves on the Riemannian manifold $\mathcal{M}$ – that we are currently investigating include: extending the notion of functional data depth from the real line $\mathbb{R}_+$ to the manifold $\mathcal{M}$, allowing for the computation of center-outward orderings of a collection of multivariate spectral curves or rank-based testing. But also, time-varying multivariate spectral estimation, and multivariate spectral estimation of replicated time series. The latter by extending the wavelet-based functional mixed-effects model proposed in [5] to the setting of multivariate replicated time series. To conclude, we mention again that the `R`-code of the wavelet-based spectral estimation and clustering algorithms including additional examples with simulated time series data is publicly available in the `R`-package `pdSpecEst`.

Acknowledgments

We thank the UC Irvine Space-Time Modeling Group, and in particular Hernando Ombao for useful discussions regarding this work, and Dr. Emad Eskandar (Massachussetts General Hospital) for the local field potential data that was used to illustrate the methodology. This research is supported by IAP research network P7/06 of the Belgian government (Belgian Science Policy), and by the contract 'Projet d'Actions de Recherche Concertées' (ARC) No. 12/17-045 of the 'Communauté française de Belgique' granted by the Académie universitaire Louvain. The first author gratefully acknowledges funding from the Belgian Fund for Scientific Research (FRIA/FRS-FNRS).

7 Appendix A: detailed proofs and algorithms

7.1 Proof of Proposition 3.1

Proof. Denote the distribution of $\mu_n := \mu_n(X_1, \ldots, X_n)$ by P_n, we show recursively that:

$$\boldsymbol{E}[\delta(\mu_n, \mu)^2] \;=\; \int_{\mathcal{M}} \delta(x, \mu)\; dP_n(x) \;\leq\; \frac{1}{n}\mathrm{Var}(X_1)$$

with $\mathrm{Var}(X_1) = \boldsymbol{E}[\delta(X_1, \mu)^2]$, the claimed result then follows by Markov's inequality.

By the generalized version of the semi-parallelogram law in [2, Theorem 6.1.9], if $X_1, X_2, X_3 \in \mathcal{M}$ are arbitrary points, then:

$$\begin{aligned}\delta(\gamma(X_1, X_2, t), X_3)^2 \;&\leq\; (1-t)\delta(X_1, X_3)^2 + t\delta(X_2, X_3)^2 \\ &\quad -t(1-t)\delta(X_1, X_2)^2, \qquad \text{for all } t \in [0,1]\end{aligned}$$

Substituting $X_3 = \mu$ and $t = 1/2$, (note that $\mathrm{Mid}(X_1, X_2) = \gamma(X_1, X_2, 1/2)$), and taking expectations on both sides yields:

$$\boldsymbol{E}_{X_1}\boldsymbol{E}_{X_2}[\delta(\mu_2, \mu)^2] \;\leq\; \frac{1}{2}\boldsymbol{E}_{X_1}[\delta(X_1, \mu)^2] + \frac{1}{2}\boldsymbol{E}_{X_2}[\delta(X_2, \mu)^2] - \frac{1}{4}\boldsymbol{E}_{X_1}\boldsymbol{E}_{X_2}[\delta(X_1, X_2)^2]$$

Using that $X_1, X_2 \overset{\text{iid}}{\sim} P$ we obtain,

$$\boldsymbol{E}[\delta(\mu_2, \mu)^2] \;\leq\; \mathrm{Var}(X_1) - \frac{1}{4}\boldsymbol{E}_{X_1}\boldsymbol{E}_{X_2}[\delta(X_1, X_2)^2] \tag{7.1}$$

From the semi-parallelogram law above, in [12, Proposition 1] the following inequality is derived:

$$\int_{\mathcal{M}} [\delta(X, Y)^2 - \delta(X, \mu)^2]\; dP(X) \;\geq\; \delta(Y, \mu)^2, \qquad \text{for any } Y \in \mathcal{M}$$

By this inequality (and using independence of X_1, X_2), the inner expectation on the right-hand side of eq.(7.1) satisfies:

$$\begin{aligned}\boldsymbol{E}_{X_2}[\delta(X_1, X_2)^2 \mid X_1 = x_1] \;&=\; \int_{\mathcal{M}} \delta(x_1, X_2)^2\; dP(X_2) \\ &\geq\; \delta(x_1, \mu)^2 + \int_{\mathcal{M}} \delta(X_2, \mu)^2\; dP(X_2) \\ &=\; \delta(x_1, \mu)^2 + \mathrm{Var}(X_2)\end{aligned}$$

and consequently,

$$\begin{aligned}\boldsymbol{E}_{X_1}\boldsymbol{E}_{X_2}[\delta(X_1, X_2)^2] \;&\geq\; \int_{\mathcal{M}} \delta(X_1, \mu)^2\; dP(X_1) + \mathrm{Var}(X_2) \\ &=\; 2\mathrm{Var}(X_1)\end{aligned}$$

Returning to eq.(7.1), we conclude that:

$$\boldsymbol{E}[\delta(\mu_2,\mu)^2] \;\leq\; \frac{1}{2}\mathrm{Var}(X_1)$$

Repeating the same argument, using the independence of $\mathrm{Mid}(X_1,X_2)$ and $\mathrm{Mid}(X_3,X_4)$, we obtain:

$$\boldsymbol{E}[\delta(\mu_4,\mu)^2] \;\leq\; \frac{1}{2}\boldsymbol{E}[\delta(\mu_2,\mu)^2] \;\leq\; \frac{1}{4}\mathrm{Var}(X_1)$$

Continuing this iteration up to μ_n, we find the upper bound:

$$\boldsymbol{E}[\delta(\mu_n,\mu)^2] \;\leq\; \frac{1}{2}\boldsymbol{E}_{n/2}[\delta(\mu_{n/2},\mu)^2] \;\leq\; \ldots \;\leq\; \frac{1}{n}\mathrm{Var}(X_1)$$

By Markov's inequality, $P(\delta(\mu_n,\mu)>\epsilon)\to 0$ for each $\epsilon>0$ as $n\to\infty$, since the distribution P is assumed to have finite second moment. □

7.2 Proof of Theorem 3.2

Proof. First, we derive the bias $b(X,f)=c(d,B)\cdot f$. By linearity of the (ordinary) expectation:

$$b(X,f) \;=\; \boldsymbol{E}[\mathrm{Log}_f(X)] \;=\; f^{1/2}*\boldsymbol{E}[\mathrm{Log}(f^{-1/2}*X)] \tag{7.2}$$

using that $g*\mathrm{Log}_{X_1}(X_2)=\mathrm{Log}_{g*X_1}(g*X_2)$ for any $g\in\mathrm{GL}(d,\mathbb{C})$. The transformed random variable $Y:=f^{-1/2}*X$ is distributed as $Y\sim W_d^c(B,B^{-1}\mathrm{I}_d)$, which is unitarily invariant (see e.g. [18, Section 3.2]). By [26, Section 2.1.5], taking the eigendecomposition of a unitarily invariant matrix $Y=Q*\Lambda$, the matrix of eigenvectors Q is distributed according to the Haar measure, the uniform distribution on the set of unitary matrices $\mathcal{U}_d=\{U\in\mathrm{GL}(d,\mathbb{C})\mid U^*U=\mathrm{I}_d\}$, implying that the eigenvectors $(\vec{q}_i)_{i=1,\ldots,d}$ (the columns of Q) are identically distributed. Furthermore, Q is independent of the diagonal eigenvalue-matrix Λ, therefore we can write (see also [24]):

$$\boldsymbol{E}[\mathrm{Log}(Y)] \;=\; \boldsymbol{E}\left[\sum_{i=1}^{d}\log(\lambda_i)\vec{q}_i\vec{q}_i^{\,*}\right] \;=\; \boldsymbol{E}[\vec{q}_i\vec{q}_i^{\,*}]\boldsymbol{E}[\log(\det(\Lambda))] \tag{7.3}$$

Since Y is Hermitian, the eigenvector matrix $Q\in\mathcal{U}_d$, and therefore $\boldsymbol{E}[\log(\det(\Lambda))] = \boldsymbol{E}[\log(\det(Y))]$. By [18, Theorem 3.2.15],

$$\log(\det(Y)) \;\sim\; -d\log(2B)+\sum_{i=1}^{d}\log\left(\chi^2_{2(B-(d-i))}\right)$$

with $\chi^2_{2(B-(d-i))}$ mutually independent chi-squared distributions, with $2(B-(d-i))$ degrees of freedom. Using that $\boldsymbol{E}[\log(\chi^2_\nu)]=\log(2)+\psi(\nu/2)$, with $\psi(\cdot)$ the digamma function, it follows that:

$$\boldsymbol{E}[\log(\det(\Lambda))] \;=\; -d\log(B)+\sum_{i=1}^{d}\psi(B-(d-i))$$

Following [24], $\boldsymbol{E}[\vec{q}_i\vec{q}_i^*] = d^{-1}\mathrm{I}_d$, thus by eq.(7.3):

$$\boldsymbol{E}[\mathrm{Log}(Y)] \;=\; \left(-\log(B) + \frac{1}{d}\sum_{i=1}^{d}\psi(B-(d-i))\right)\mathrm{I}_d \;=\; c(d,B)\cdot\mathrm{I}_d$$

Plugging this back into eq.(7.2) yields the claimed result $b(X,f) = c(d,B)\cdot f$.

For the second part of the theorem, we observe that $\widetilde{X}_\ell$ (for $1 \le \ell \le n$) is unbiased with respect to f, since:

$$\begin{aligned} b(\widetilde{X}_\ell, f) &= f^{1/2} * \boldsymbol{E}[\mathrm{Log}(f^{-1/2} * \widetilde{X}_\ell)] \\ &= f^{1/2} * \boldsymbol{E}[\mathrm{Log}(e^{-c(d,B)}\mathrm{I}_d) + \mathrm{Log}(f^{-1/2} * X_\ell)] \\ &= f^{1/2} * (-c(d,B)\mathrm{I}_d + c(d,B)\mathrm{I}_d) \;=\; \mathbf{0}_{d\times d} \end{aligned}$$

where we used that $\mathrm{Log}(AB) = \mathrm{Log}(A) + \mathrm{Log}(B)$ for commuting matrices A, B, and the fact that $\boldsymbol{E}[\mathrm{Log}(f^{-1/2} * X_\ell)] = c(d,B)\cdot\mathrm{I}_d$ as derived above. By [20], the unique Karcher mean of $\widetilde{X}_\ell$ on $\mathcal{M}$ is characterized by μ such that $b(\widetilde{X}_\ell, f) = \boldsymbol{E}[\mathrm{Log}_\mu(\widetilde{X}_\ell)] = \mathbf{0}_{d\times d}$. Therefore we conclude that f is the unique Karcher mean of $\widetilde{X}_\ell$ for each $\ell = 1,\ldots,n$, since the distribution of $\widetilde{X}_\ell$ has finite second moment (rescaled complex Wishart distribution), the claimed result follows by Proposition 3.1. □

7.3 Proof of Proposition 3.3

Proof. Let us write $M^X_{J,k-1} := X_k = f_k^{1/2} * W_k$ for $k = 1,\ldots,n$, where the distribution of W_k does not depend on f_k, and the Karcher mean of W_k is equal to I_d. The latter follows from the fact that X_k has Karcher mean f_k, since:

$$\begin{aligned} \boldsymbol{E}[\mathrm{Log}_{\mathrm{I}_d}(W_k)] &= \boldsymbol{E}[f_k^{-1/2} * \mathrm{Log}_{f_k}(f_k^{1/2} * W_k)] \\ &= f_k^{1/2} * \boldsymbol{E}[\mathrm{Log}_{f_k}(X_k)] \\ &= f_k^{1/2} * \mathbf{0}_{d\times d} \;=\; \mathbf{0}_{d\times d} \end{aligned}$$

and the Karcher mean μ of W_k is uniquely characterized by $\boldsymbol{E}[\mathrm{Log}_\mu(W_k)] = \mathbf{0}_{d\times d}$. First, we show that:

$$\mathrm{Tr}(\mathrm{Log}(M^X_{j,k})) \;=\; \mathrm{Tr}(\mathrm{Log}(M^f_{j,k})) + \mathrm{Tr}(\mathrm{Log}(M^W_{j,k}))$$

where $M^X_{j,k}$, $M^f_{j,k}$, and $M^W_{j,k}$ are the midpoints at scale-location (j,k) based on the sequences $(X_\ell)_\ell$, $(f_\ell)_\ell$, and $(W_\ell)_\ell$ respectively. Using the identities $\mathrm{Tr}(\mathrm{Log}(AB)) = \mathrm{Tr}(\mathrm{Log}(A)) +$

$\mathrm{Tr}(\mathrm{Log}(B))$ and $\mathrm{Log}(A^t) = t\mathrm{Log}(A)$ for any $A, B \in \mathcal{M}$, we decompose:

$$\begin{aligned}
\mathrm{Tr}(\mathrm{Log}(M^X_{j,k})) &= \mathrm{Tr}(\mathrm{Log}(\mathrm{Mid}\{M^X_{j+1,2k}, M^X_{j+1,2k+1}\})) \\
&= \mathrm{Tr}\big(\mathrm{Log}\big((M^X_{j+1,2k})^{1/2} * \big((M^X_{j+1,2k})^{-1/2} * M^X_{j+1,2k+1}\big)^{1/2}\big)\big) \\
&= \frac{1}{2}\mathrm{Tr}(\mathrm{Log}(M^X_{j+1,2k})) + \frac{1}{2}\mathrm{Tr}(\mathrm{Log}(M^X_{j+1,2k+1})) \\
&\vdots \\
&= \sum_{\ell=0}^{2^{J-j-1}-1} \mathrm{Tr}(\mathrm{Log}(M^X_{J,(2k)^{J-j-1}+\ell})) \\
&= \sum_{\ell=0}^{2^{J-j-1}-1} \mathrm{Tr}(\mathrm{Log}(f_{(2k)^{J-j-1}+\ell+1})) + \sum_{\ell=0}^{2^{J-j-1}-1} \mathrm{Tr}(\mathrm{Log}(W_{(2k)^{J-j-1}+\ell+1})) \\
&\vdots \\
&= \mathrm{Tr}(\mathrm{Log}(\mathrm{Mid}(M^f_{j+1,2k}, M^f_{j+1,2k+1}))) + \mathrm{Tr}(\mathrm{Log}(\mathrm{Mid}(M^W_{j+1,2k}, M^W_{j+1,2k+1}))) \\
&= \mathrm{Tr}(\mathrm{Log}(M^f_{j,k})) + \mathrm{Tr}(\mathrm{Log}(M^W_{j,k})) \qquad (7.4)
\end{aligned}$$

Second, we also show that:

$$\mathrm{Tr}(\mathrm{Log}(\widetilde{M}^X_{j+1,2k+1})) = \mathrm{Tr}(\mathrm{Log}(\widetilde{M}^f_{j+1,2k+1})) + \mathrm{Tr}(\mathrm{Log}(\widetilde{M}^W_{j+1,2k+1}))$$

where $\widetilde{M}^X_{j,k}, \widetilde{M}^f_{j,k}$, and $\widetilde{M}^W_{j,k}$ are the imputed midpoints at scale-location (j,k) based on the sequences $(X_\ell)_\ell$, $(f_\ell)_\ell$, and $(W_\ell)_\ell$ respectively. As noted in [9], the imputed values $\tilde{\theta}^i_{j+1,2k}, \tilde{\theta}^i_{j+1,2k+1} \in \mathbb{R}$ for each $i = 1, \ldots, d^2$ can be expressed as kernel weighted averages of the observations $(\theta^i_{j,k+\ell})_{-D\le\ell\le D}$, with kernel weights $(K^{\mathrm{even}}_\ell)_\ell$, $(K^{\mathrm{odd}}_\ell)_\ell$ depending on the order $N = 2D+1$ of the refinement scheme, i.e.

$$\widetilde{\theta}^i_{j+1,2k} = \sum_{-D\le\ell\le D} K^{\mathrm{even}}_\ell \theta^i_{j,k+\ell}, \qquad \widetilde{\theta}^i_{j+1,2k+1} = \sum_{-D\le\ell\le D} K^{\mathrm{odd}}_\ell \theta^i_{j,k+\ell}$$

It follows that the imputed midpoints $\widetilde{M}_{j+1,2k+1}$ at the odd locations (analogous for the even locations $2k$) can be expressed as:

$$\widetilde{M}_{j+1,2k+1} = \mathrm{Exp}_{M_{j,k}}\left(\sum_{-D\le\ell\le D} K^{\mathrm{odd}}_\ell \mathrm{Log}_{M_{j,k}}(M_{j,k+\ell})\right)$$

Writing $K_\ell = K_\ell^{\text{odd}}$ for notational convenience, using eq.(7.4) we can decompose:

$$\begin{aligned}
\mathrm{Tr}(\mathrm{Log}(\widetilde{M}^X_{j+1,2k+1})) &= \mathrm{Tr}\Big(\mathrm{Log}\Big(\mathrm{Exp}_{M^X_{j,k}}\Big(\sum_\ell K_\ell \mathrm{Log}_{M^X_{j,k}}(M^X_{j,k+\ell})\Big)\Big)\Big) \\
&= \mathrm{Tr}(\mathrm{Log}(M^X_{j,k})) + \mathrm{Tr}\left((M^X_{j,k})^{-1/2} * \Big(\sum_\ell K_\ell \mathrm{Log}_{M^X_{j,k}}(M^X_{j,k+\ell})\Big)\right) \\
&= \mathrm{Tr}(\mathrm{Log}(M^X_{j,k})) + \mathrm{Tr}\left(\sum_\ell K_\ell \mathrm{Log}\Big((M^X_{j,k})^{-1/2} * M^X_{j,k+\ell}\Big)\right) \\
&= \mathrm{Tr}(\mathrm{Log}(M^X_{j,k})) + \sum_\ell K_\ell \left(\mathrm{Tr}(\mathrm{Log}(M^X_{j,k+\ell})) - \mathrm{Tr}(\mathrm{Log}(M^X_{j,k}))\right) \\
&= \mathrm{Tr}(\mathrm{Log}(M^f_{j,k})) + \sum_\ell K_\ell \Big(\mathrm{Tr}(\mathrm{Log}(M^f_{j,k+\ell})) - \mathrm{Tr}(\mathrm{Log}(M^f_{j,k}))\Big) \\
&\quad + \mathrm{Tr}(\mathrm{Log}(M^W_{j,k})) + \sum_\ell K_\ell \left(\mathrm{Tr}(\mathrm{Log}(M^W_{j,k+\ell})) - \mathrm{Tr}(\mathrm{Log}(M^W_{j,k}))\right) \\
&\ \ \vdots \\
&= \mathrm{Tr}(\mathrm{Log}(\widetilde{M}^f_{j+1,2k+1})) + \mathrm{Tr}(\mathrm{Log}(\widetilde{M}^W_{j+1,2k+1})) \qquad (7.5)
\end{aligned}$$

where we used (among other steps) that $g{*}\mathrm{Log}_{X_1}(X_2) = \mathrm{Log}_{g*X_1}(g{*}X_2)$ and $g{*}\mathrm{Exp}_{X_1}(X_2) = \mathrm{Exp}_{g*X_1}(g * X_2)$ for any $g \in \mathrm{GL}(d,\mathbb{C})$.

The first claim in the Proposition now follows from eq.(7.4) and eq.(7.5) through:

$$\begin{aligned}
\mathrm{Tr}(D^X_{j,k}) &= \mathrm{Tr}\Big(\mathrm{Log}\Big((\widetilde{M}^X_{j+1,2k+1})^{-1/2} * M^X_{j+1,2k+1}\Big)\Big) \\
&= \mathrm{Tr}(\mathrm{Log}(M^X_{j+1,2k+1})) - \mathrm{Tr}(\mathrm{Log}(\widetilde{M}^X_{j+1,2k+1})) \\
&= \mathrm{Tr}(\mathrm{Log}(M^f_{j+1,2k+1})) + \mathrm{Tr}(\mathrm{Log}(M^W_{j+1,2k+1})) \\
&\quad - \Big(\mathrm{Tr}(\mathrm{Log}(\widetilde{M}^f_{j+1,2k+1})) + \mathrm{Tr}(\mathrm{Log}(\widetilde{M}^W_{j+1,2k+1}))\Big) \\
&= \mathrm{Tr}(D^f_{j,k}) + \mathrm{Tr}(D^W_{j,k}) \qquad (7.6)
\end{aligned}$$

In order to prove the second claim in the Proposition, we first observe that:

$$\boldsymbol{E}[\mathrm{Tr}(\mathrm{Log}(M^W_{j,k}))] \;=\; \sum_{\ell=0}^{2^{J-j-1}-1} \boldsymbol{E}[\mathrm{Tr}(\mathrm{Log}(W_{(2k)^{J-j-1}+\ell+1}))] \;=\; 0, \qquad \text{for each } j,k$$

using that $\boldsymbol{E}[\mathrm{Tr}(\mathrm{Log}(W_\ell))] = 0$ for each $\ell = 1,\ldots,n$, which is implied by $\boldsymbol{E}[\mathrm{Log}_{\mathrm{I}_d}(W_\ell)] = \mathbf{0}_{d\times d}$. As a consequence,

$$\begin{aligned}
&\boldsymbol{E}[\mathrm{Tr}(\mathrm{Log}(\widetilde{M}^W_{j+1,2k+1}))] \\
&\qquad = \boldsymbol{E}[\mathrm{Tr}(\mathrm{Log}(M^W_{j,k}))] + \sum_\ell K_\ell \left(\boldsymbol{E}[\mathrm{Tr}(\mathrm{Log}(M^W_{j,k+\ell}))] - \boldsymbol{E}[\mathrm{Tr}(\mathrm{Log}(M^W_{j,k}))]\right) \\
&\qquad = 0
\end{aligned}$$

and therefore,

$$\begin{aligned}\boldsymbol{E}[\mathrm{Tr}(D^X_{j,k})] &= \mathrm{Tr}(D^f_{j,k}) + \boldsymbol{E}[\mathrm{Tr}(D^W_{j,k})] \\ &= \mathrm{Tr}(D^f_{j,k}) + \boldsymbol{E}\left[\mathrm{Tr}(\mathrm{Log}(M^W_{j+1,2k+1})) - \mathrm{Tr}(\mathrm{Log}(\widetilde{M}^W_{j+1,2k+1}))\right] \\ &= \mathrm{Tr}(D^f_{j,k})\end{aligned}$$

For the variance of $\mathrm{Tr}(D^X_{j,k})$, we first note that the random variables $(W_\ell)_{\ell=1,\ldots,n}$ are i.i.d., implying that the random variables $(\mathrm{Tr}(\mathrm{Log}(M^W_{j,k}))_{k=0,\ldots,2^j-1}$ on scale j are independent with equal variance. We write out:

$$\begin{aligned}\mathrm{Var}(\mathrm{Tr}(D^X_{j,k})) &= \mathrm{Var}\left(\mathrm{Tr}(\mathrm{Log}(M^W_{j+1,2k+1})) - \mathrm{Tr}(\mathrm{Log}(\widetilde{M}^W_{j+1,2k+1}))\right) \\ &= \mathrm{Var}\left(\mathrm{Tr}(\mathrm{Log}(M^W_{j+1,2k+1})) - \sum_{-D\le\ell\le D} K_\ell \mathrm{Tr}(\mathrm{Log}(M^W_{j,k+\ell}))\right) \\ &= \mathrm{Var}\left(\mathrm{Tr}(\mathrm{Log}(M^W_{j+1,2k+1})) - K_0\mathrm{Tr}(\mathrm{Log}(M^W_{j,k}))\right) \\ &\quad + \sum_{-D\le\ell\le D;\ell\neq 0} K^2_\ell \mathrm{Var}(\mathrm{Tr}(\mathrm{Log}(M^W_{j,k+\ell}))) \\ &= \frac{1}{2}\mathrm{Var}(\mathrm{Tr}(\mathrm{Log}(M^W_{j+1,2k})) + \Big(\sum_{-D\le\ell\le D} K^2_\ell - 1\Big)\mathrm{Var}(\mathrm{Tr}(\mathrm{Log}(M^W_{j,k+\ell}))) \\ &= \sum_{-D\le\ell\le D}\frac{1}{2}K^2_\ell \mathrm{Var}(\mathrm{Tr}(\mathrm{Log}(M^W_{j+1,1}))) \qquad (7.7)\end{aligned}$$

where in the last two steps we used that $K_0 = 1$ if $N > 1$, with N is the order of the refinement scheme, and by the independence of the midpoints within each scale:

$$\begin{aligned}\mathrm{Var}(\mathrm{Tr}(\mathrm{Log}(M^W_{j,k}))) &= \mathrm{Var}\left(\frac{1}{2}\mathrm{Tr}(\mathrm{Log}(M^W_{j+1,2k})) + \frac{1}{2}\mathrm{Tr}(\mathrm{Log}(M^W_{j+1,2k+1}))\right) \\ &= \frac{1}{2}\mathrm{Var}(\mathrm{Tr}(\mathrm{Log}(M^W_{j+1,1})) \qquad (7.8)\end{aligned}$$

It remains to derive an expression for $\mathrm{Var}(\mathrm{Tr}(\mathrm{Log}(M^W_{j+1,1})))$. By multiple applications of the argument in eq.(7.8), we observe that:

$$\begin{aligned}\mathrm{Var}(\mathrm{Tr}(\mathrm{Log}(M^W_{j+1,1}))) &= \frac{1}{2^{J-j-1}}\mathrm{Var}(\mathrm{Tr}(\mathrm{Log}(M^W_{J,1}))) \\ &= \frac{1}{2^{J-j-1}}\mathrm{Var}(\mathrm{Tr}(\mathrm{Log}(W_1))) \qquad (7.9)\end{aligned}$$

with $W_1 \sim W^c_d(B, B^{-1}e^{-c(d,B)}\mathrm{I}_d)$. As in the proof of Theorem 3.2,

$$\mathrm{Tr}(\mathrm{Log}(W_1)) \sim -d\log(2e^{c(d,B)}B) + \sum_{i=1}^{d}\log\left(\chi^2_{2(B-(d-i))}\right)$$

and since the variance of $\log(\chi^2_\nu)$ equals $\psi'(\nu/2)$, where $\psi'(\cdot)$ denotes the trigamma function, it follows that:

$$\mathrm{Var}(\mathrm{Tr}(\mathrm{Log}(W_1)) = \sum_{i=1}^{d}\psi'(B-(d-i))$$

Combining the above result with eq.(7.9) and eq.(7.7) finishes the proof. □

7.4 Proof of Corollary 3.4

Proof. First, we show that the random wavelet coefficients $D^W_{j,k}$ are unitarily invariant. As in the proof of Theorem 3.2, we start by noting that the random variables $W_1, \ldots, W_n \overset{\text{iid}}{\sim} W_d^c(B, B^{-1}e^{-c(d,B)}\mathrm{I}_d)$ are unitarily invariant, see [18, Section 3.2]. The midpoint of two such random variables is again unitarily invariant, since for any unitary matrix $U \in \mathcal{U}_d$,

$$\begin{aligned} U * M^W_{J-1,k} &= U * \mathrm{Mid}(W_{2k+1}, W_{2k+2}) \\ &= \mathrm{Mid}(U * W_{2k+1}, U * W_{2k+2}) \\ &\overset{d}{=} \mathrm{Mid}(W_{2k+1}, W_{2k+2}) \;=\; M^W_{J-1,k} \end{aligned}$$

using that $g * \mathrm{Mid}(X_1, X_2) = \mathrm{Mid}(g * X_1, g * X_2)$ for any $g \in \mathrm{GL}(d, \mathbb{C})$. Iteration of the same argument, shows that $U * M^W_{j,k} \overset{d}{=} M^W_{j,k}$ for each $1 \leq j \leq J$. By the fact that the repeated midpoints are unitarily invariant, it follows that the imputed midpoints are unitarily invariant as well, since for any $U \in \mathcal{U}_d$,

$$\begin{aligned} U * \widetilde{M}^W_{j+1,2k+1} &= U * \mathrm{Exp}_{M^W_{j,k}}\left(\sum_\ell K_\ell \mathrm{Log}_{M^W_{j,k}}\left(M^W_{j,k+\ell}\right)\right) \\ &= \mathrm{Exp}_{U*M^W_{j,k}}\left(\sum_\ell K_\ell \mathrm{Log}_{U*M^W_{j,k}}\left(U * M^W_{j,k+\ell}\right)\right) \\ &\overset{d}{=} \widetilde{M}^W_{j+1,2k+1} \end{aligned}$$

using that $g * \mathrm{Log}_{X_1}(X_2) = \mathrm{Log}_{g*X_1}(g * X_2)$ and $g * \mathrm{Exp}_{X_1}(X_2) = \mathrm{Exp}_{g*X_1}(g * X_2)$ for any $g \in \mathrm{GL}(d, \mathbb{C})$. Combining the above results, it follows that the random wavelet coefficient $D^W_{j,k}$ is unitarily invariant, as for each $U \in \mathcal{U}_d$, we can write out:

$$\begin{aligned} U * D^W_{j,k} &= U * \mathrm{Log}\left((\widetilde{M}^W_{j+1,2k+1})^{-1/2} * M_{j+1,2k+1}\right) \\ &= \mathrm{Log}\left((U * \widetilde{M}^W_{j+1,2k+1})^{-1/2} * (U * M_{j+1,2k+1})\right) \\ &\overset{d}{=} \mathrm{Log}\left((\widetilde{M}^W_{j+1,2k+1})^{-1/2} * M_{j+1,2k+1}\right) \\ &= D^W_{j,k} \end{aligned}$$

using that $U * \mathrm{Log}(X) = \mathrm{Log}(U * X)$ for $U \in \mathcal{U}_d$. By the same argument as in Theorem 3.2, if we write the eigendecomposition $D^W_{j,k} = Q * \Lambda$, then for a unitarily invariant random matrix $D^W_{j,k}$, we have that:

$$\begin{aligned} \boldsymbol{E}[D^W_{j,k}] &= \boldsymbol{E}\left[\sum_{i=1}^d \lambda_i \vec{q}_i \vec{q}_i^*\right] \\ &= \boldsymbol{E}[\vec{q}_i \vec{q}_i^*]\boldsymbol{E}[\mathrm{Tr}(\Lambda)] \\ &= \boldsymbol{E}[\vec{q}_i \vec{q}_i^*]\boldsymbol{E}[\mathrm{Tr}(D^W_{j,k})] \;=\; \mathbf{0}_{d\times d} \end{aligned}$$

Here we used that $\mathrm{Tr}(Q * \Lambda) = \mathrm{Tr}(\Lambda)$, since Q is a unitary matrix, which follows from the fact that $D^W_{j,k}$ is Hermitian. □

7.5 Proof of Proposition 3.5

Proof. Using the same notation as in the proof of Proposition 3.3, we first show that the midpoints $(M^X_{j,k+\ell})_{-D\leq\ell\leq D}$ satisfy the relation:

$$M^X_{j,k+\ell} \;=\; f^{1/2}_{j,k} * M^W_{j,k+\ell}, \qquad \text{for } -D \leq \ell \leq D \tag{7.10}$$

where $f_{j,k}$ is the locally constant spectrum $(f_i)_i$ for $i \in \{2^{J-j}(k-D)+1, \ldots, 2^{J-j}(k+D+1)\}$. To see this, we write out:

$$\begin{aligned} M^X_{j,k+i} &= \mu_{2^{J-j}}\left(M^X_{J,2^{J-j}(k+i)}, \ldots, M^X_{J,2^{J-j}(k+i+1)-1}\right) \\ &= \mu_{2^{J-j}}\left(f^{1/2}_{j,k} * W_{2^{J-j}(k+i)+1}, \ldots, f^{1/2}_{j,k} * W_{2^{J-j}(k+i+1)}\right) \\ &= f^{1/2}_{j,k} * \mu_{2^{J-j}}\left(W_{2^{J-j}(k+i)+1}, \ldots, W_{2^{J-j}(k+i+1)}\right) \\ &= f^{1/2}_{j,k} * M^W_{j,k+i} \end{aligned}$$

where we used the notation for the repeated midpoint functional as in Section 3.1, and recursive applications of the identity $\mathrm{Mid}(g * X_1, g * X_2) = g * \mathrm{Mid}(X_1, X_2)$ for any $g \in \mathrm{GL}(d, \mathbb{C})$. Note that in particular also $M^X_{j+1,2k+1} = f^{1/2}_{j,k} * M^W_{j+1,2k+1}$, which is used in eq.(7.11) below.

The same relation holds for the imputed midpoint $\widetilde{M}^X_{j+1,2k+1}$, since:

$$\begin{aligned} \widetilde{M}^X_{j+1,2k+1} &= \mathrm{Exp}_{f^{1/2}_{j,k} * M^W_{j,k}}\left(\sum_{-D\leq\ell\leq D} K_\ell \mathrm{Log}_{f^{1/2}_{j,k} * M^W_{j,k}}(f^{1/2}_{j,k} * M^W_{j,k+\ell})\right) \\ &= \mathrm{Exp}_{f^{1/2}_{j,k} * M^W_{j,k}}\left(f^{1/2}_{j,k} * \left(\sum_{-D\leq\ell\leq D} K_\ell \mathrm{Log}_{M^W_{j,k}}(M^W_{j,k+\ell})\right)\right) \\ &= f^{1/2}_{j,k} * \widetilde{M}^W_{j+1,2k+1} \end{aligned}$$

by eq.(7.10) above, and using the identities $\mathrm{Exp}_{g*X_1}(g*X_2) = g*\mathrm{Exp}_{X_1}(X_2)$ and $\mathrm{Log}_{g*X_1}(g*X_2) = g * \mathrm{Log}_{X_1}(X_2)$ for $g \in \mathrm{GL}(d, \mathbb{C})$.

By definition of the wavelet coefficient $D^X_{j,k}$ and the Riemannian distance function, it now

follows that with $p \in \mathbb{R}$,

$$\begin{aligned}
\boldsymbol{E}\|D^X_{j,k}\|_F^p &= \boldsymbol{E}\left\|\mathrm{Log}\left((\widetilde{M}^X_{j+1,2k+1})^{-1/2} * M^X_{j+1,2k+1}\right)\right\|_F^p \\
&= \boldsymbol{E}\left[\delta\left(\widetilde{M}^X_{j+1,2k+1}, M^X_{j+1,2k+1}\right)^p\right] \\
&= \boldsymbol{E}\left[\delta\left(f^{1/2}_{j,k} * \widetilde{M}^W_{j+1,2k+1}, f^{1/2}_{j,k} * M^W_{j+1,2k+1}\right)^p\right] \\
&= \boldsymbol{E}\left[\delta\left(\widetilde{M}^W_{j+1,2k+1}, M^W_{j+1,2k+1}\right)^p\right] \\
&= \boldsymbol{E}\|D^W_{j,k}\|_F^p \qquad (7.11)
\end{aligned}$$

using the fact that the Riemannian distance is invariant to congruence transformation by $f^{1/2}_{j,k} \in \mathrm{GL}(d,\mathbb{C})$, as described in Section 2. □

7.6 Proof of Proposition 3.6

Proof. Using the same notation as in the proof of Proposition 3.3, let $(M^{X,\pi}_{j,k})_{j,k}$ be the midpoints under the permuted ordering of the components, such that $M^{X,\pi}_{J,k-1} = X^\pi_k = U_\pi * X_k = U_\pi * M^X_{J,k-1}$, where U_π denotes the (unitary) permutation matrix corresponding to the permutation $\pi(1,\ldots,d)$. By repeated application of the identity $\mathrm{Mid}(U_\pi * A, U_\pi * B) = U_\pi * \mathrm{Mid}(A,B)$, it follows that:

$$M^{X,\pi}_{j,k} = U_\pi * M^X_{j,k}, \qquad \text{for all } j,k \qquad (7.12)$$

The same holds true for the imputed midpoints, i.e. $\widetilde{M}^{X,\pi}_{j+1,2k+1} = U_\pi * \widetilde{M}^X_{j+1,2k+1}$ for all j,k. The argument, using eq.(7.12), is essentially the same as in the proof of Proposition 3.5. As a consequence, for the wavelet coefficients $(D^{X,\pi}_{j,k})_{j,k}$, we have:

$$\begin{aligned}
D^{X,\pi}_{j,k} &= \mathrm{Log}\left((U_\pi * \widetilde{M}^X_{j+1,2k+1})^{-1/2} * (U_\pi * M^X_{j+1,2k+1}\right) \\
&= \mathrm{Log}\left(U_\pi * \left((\widetilde{M}^X_{j+1,2k+1})^{-1/2} * M^X_{j+1,2k+1})\right)\right) \\
&= U_\pi * D^X_{j,k} \qquad (7.13)
\end{aligned}$$

where we used that $(U * X)^t = U * X^t$ and $\mathrm{Log}(U * X) = U * \mathrm{Log}(X)$ for $t \in \mathbb{R}$ and $U \in \mathcal{U}_d$.

To compute the spectral estimator, we threshold the components of the wavelet coefficients expanded into the orthonormal basis $(E_i)_{i=1,\ldots,d^2}$ of $\mathcal{H}$, such that:

$$\begin{aligned}
\sum_{i=1}^{d^2} d^{X,\pi,i}_{j,k} E_i = D^{X,\pi}_{j,k} &= U_\pi * D^X_{j,k} \\
&= U_\pi * \left(\sum_{i=1}^{d^2} d^{X,i}_{j,k} E_i\right) = \sum_{i=1}^{d^2} d^{X,i}_{j,k} (U_\pi * E_i)
\end{aligned}$$

The set of basis elements $(U_\pi * E_i)_{i=1,\ldots,d^2}$ is just a permutation of the original set $(E_i)_{i=1,\ldots,d^2}$, (with possibly the conjugate transpose for the complex-valued basis matrices). Suppose that

$\sigma(\vec{\lambda}) = \sigma(\lambda_1, \ldots, \lambda_{d^2})$ is the permutation of the thresholds corresponding to the permutation of the basis elements in $(U_\pi * E_i)_{i=1,\ldots,d^2}$. For each $i = 1, \ldots, d^2$, the hard thresholded components are given by,

$$d_{j,k}^{\hat{f},\pi,i} \;=\; d_{j,k}^{X,\pi,i} \mathbf{1}\{|\tilde{d}_{j,k}^{X,\pi,i}| > \sigma(\vec{\lambda})_i\}, \qquad \text{for each } j,k$$

where $\tilde{d}_{j,k}^{X,\pi,i} = c_j d_{j,k}^{X,\pi,i}$ is the wavelet coefficient with normalized variance, where the scaling factor c_j depends only on the wavelet scale j. Similarly for the non-permuted versions:

$$d_{j,k}^{\hat{f},i} \;=\; d_{j,k}^{X,i} \mathbf{1}\{|\tilde{d}_{j,k}^{X,i}| > \lambda_i\}, \qquad \text{for each } j,k$$

with $\tilde{d}_{j,k}^{X,i} = c_j d_{j,k}^{X,i}$ the normalized wavelet coefficient. Note that the components $(d_{j,k}^{X,i})_i$ may differ in sign with respect to their permuted counterparts $(d_{j,k}^{X,\pi,i})_{\sigma(i)}$, but for the thresholding this does not matter as the absolute values are sign independent. By recomposition of the thresholded wavelet coefficients, it is seen that the same relation as in eq.(7.13) for the non-thresholded wavelet coefficients holds true,

$$\begin{aligned} D_{j,k}^{\hat{f},\pi} \;=\; \sum_{i=1}^{d^2} d_{j,k}^{\hat{f},\pi,i} E_i \;&=\; \sum_{i=1}^{d^2} d_{j,k}^{\hat{f},i} (U_\pi * E_i) \\ &=\; U_\pi * \left(\sum_{i=1}^{d^2} d_{j,k}^{\hat{f},i} E_i \right) \;=\; U_\pi * D_{j,k}^{\hat{f},i} \end{aligned}$$

The wavelet-thresholded spectral estimator $\hat{f}_{\sigma(\vec{\lambda}),\pi}(\omega_\ell)$ is retrieved via the inverse wavelet transform applied to the set of thresholded wavelet coefficients (and coarse-scale midpoints). At scale $j = 1$, the estimated midpoints $M_{1,k}^{\hat{f},\pi}$ are taken to be equal to the observed midpoints $M_{1,k}^{X,\pi}$, and by eq.(7.12), $M_{1,k}^{\hat{f},\pi} = M_{1,k}^{X,\pi} = U_\pi * M_{1,k}^X = U_\pi * M_{1,k}^{\hat{f}}$ for $k = 0, 1$. At the next coarser scale $j+1$, the estimated midpoints at the odd locations $2k+1$ satisfy:

$$\begin{aligned} M_{j+1,2k+1}^{\hat{f},\pi} \;&=\; \widetilde{M}_{j+1,2k+1}^{\hat{f},\pi} * \mathrm{Exp}(D_{j,k}^{\hat{f},\pi}) \\ &=\; (U_\pi * \widetilde{M}_{j+1,2k+1}^{\hat{f}}) * \mathrm{Exp}(U_\pi * D_{j,k}^{\hat{f}}) \\ &=\; U_\pi * M_{j+1,2k+1}^{\hat{f}} \end{aligned}$$

where the claim $\widetilde{M}_{j+1,2k+1}^{\hat{f},\pi} = U_\pi * \widetilde{M}_{j+1,2k+1}^{f}$ is seen to be true by noting that it is true at scale j, and using the same argument as in the proof of Proposition 3.5. Also, for the estimated midpoints at the even locations $2k$,

$$\begin{aligned} M_{j+1,2k}^{\hat{f},\pi} \;&=\; (U_\pi * M_{j,k}^{\hat{f},\pi}) * (U_\pi * M_{j+1,2k+1}^{\hat{f},\pi})^{-1} \\ &=\; U_\pi * \left(M_{j,k}^{\hat{f},\pi} * (M_{j+1,2k+1}^{\hat{f},\pi})^{-1} \right) \\ &=\; U_\pi * M_{j+1,2k}^{\hat{f}} \end{aligned}$$

using that $(U * X)^t = U * X^t$ for $t \in \mathbb{R}$ and $U \in \mathcal{U}_d$. Iterating the above arguments up to the finest scale $j = J$ yields the desired result,

$$\hat{f}_{\sigma(\vec{\lambda}),\pi}(\omega_{k+1}) \;=\; M_{J,k}^{\hat{f},\pi} \;=\; U_\pi * M_{J,k}^{\hat{f}} \;=\; U_\pi * \hat{f}_{\vec{\lambda}}(\omega_{k+1})$$

for each $k = 0, \ldots, 2^J - 1$. □

7.7 Details on clustering algorithms in Section 4

Geometric fuzzy c-means algorithm We describe the fuzzy c-means algorithm based on the Riemannian distance function used to minimize the WCSSD functional in eq.(4.1) corresponding to step 2. of the clustering algorithm in Section 4, see also [1].

Step 1. Initialize cluster centers $(\overline{M}_{1,0}^{k,(0)}, \overline{M}_{1,1}^{k,(0)})_{k=1,\ldots,K}$ for the K clusters, by randomly sampling K midpoint vectors (i.e. feature vectors) from the collection of S midpoint vectors $(M_{1,0}^s, M_{1,1}^s)_{s=1,\ldots,S}$.

Step 2. At iteration $\ell = 0, \ldots,$ compute the distances:

$$\mathrm{dist}_{sk}^{(\ell)} \;=\; \sum_{i=0}^{1} \delta(M_{1,i}^s, \overline{M}_{1,i}^{k,(\ell)})^2$$

Step 3. Update the $S \times K$-dimensional partition matrix $U^{(\ell)}$ with elements $u_{sk}^{(\ell)}$,
for $1 \le s \le S$,
if $\mathrm{dist}_{sk}^{(\ell)} > 0$ for each $k = 1, \ldots, K$, set

$$u_{sk}^{(\ell)} \;=\; \frac{(\mathrm{dist}_{sk}^{(\ell)})^{-\frac{1}{m-1}}}{\sum_{q=1}^{K} (\mathrm{dist}_{sq}^{(\ell)})^{-\frac{1}{m-1}}}$$

with $m \in (1, \infty)$ the fuzziness parameter.
otherwise set $u_{sk}^{(\ell)} = 0$ for each k with $\mathrm{dist}_{sk}^{(\ell)} > 0$, and set

$$u_{sk}^{(\ell)} \;=\; \frac{1}{\|(\mathrm{dist}_{sk}^{(\ell)})_k\|_0}$$

for each k with $\mathrm{dist}_{sk}^{(\ell)} = 0$, where $\|\boldsymbol{x}\|_0 = \#\{k : x_k = 0\}$.

Step 4. For each $k = 1, \ldots, K$, compute the new cluster centers $\overline{M}_{1,0}^{k,(\ell+1)}$ and $\overline{M}_{1,1}^{k,(\ell+1)}$ via the (approximate) empirical weighted Karcher mean of $(M_{1,0}^s)_s$ and $(M_{1,1}^s)_s$ as in eq.(4.3) or eq.(4.4) based on the weights:

$$\mathrm{weight}_{sk}^{(\ell)} \;=\; \frac{(u_{sk}^{(\ell)})^m}{\sum_{r=1}^{S} (u_{rk}^{(\ell)})^m}, \qquad \text{for } s = 1, \ldots, S$$

Step 5. Terminate when,

$$\sum_{k=1}^{K}\sum_{i=0}^{1}\delta\Big(\overline{M}_{1,i}^{k,(\ell)},\overline{M}_{1,i}^{k,(\ell+1)}\Big)^2<\epsilon$$

for some small value of ϵ, otherwise return to Step 2.

Weighted fuzzy c-means algorithm We also describe the weighted fuzzy c-means algorithm based on the Euclidean (i.e. Frobenius) distance used to minimize the WCSSD functional in eq.(4.5) corresponding to step 3. of the clustering algorithm in Section 4.

Step 1. Initialize cluster centers $(\overline{D}_{j,i}^{k,(0)})_{k,j,i}$ with $k=1,\ldots,K$, $j=1,\ldots,j_{\max}$, and $i=0,\ldots,2^j-1$. Here, the cluster center $\overline{D}_{j,i}^{k,(0)}$ is an (ordinary) weighted Euclidean mean of the observations $(D_{j,i}^s)_s$, with weights:

$$\text{weight}_{sk}^{(-1)} \;=\; \frac{(u_{sk}^{(-1)})^m}{\sum_{r=1}^{S}(u_{sk}^{(-1)})^m},\qquad \text{for } s=1,\ldots,S$$

where $m\in(1,\infty)$ is the fuzziness parameter. The weight matrix $U^{(-1)}$ is the fuzzy partition matrix obtained at the final iteration of the geometric fuzzy c-means algorithm detailed above.

Step 2. At iteration $\ell=0,\ldots,$ compute the distances:

$$\text{dist}_{sk}^{(\ell)} \;=\; \sum_{j=1}^{j_{\max}}\sum_{i=0}^{2^j-1} w_{jsk}\|D_{j,i}^s-\overline{D}_{j,i}^{k,(\ell)}\|_F^2$$

with $w_{jsk}=2^{(j_{\max}-j)}\frac{1-\exp(-\tau\text{dist}_{sk}^{(-1)})}{1+\exp(-\tau\text{dist}_{sk}^{(-1)})}$, where $(\text{dist}_{sk}^{(-1)})_{s,k}$ are the distances obtained at the final iteration of the geometric fuzzy c-means algorithm detailed above.

Step 3. Update the $S\times K$-dimensional partition matrix $U^{(\ell)}$ with elements $u_{sk}^{(\ell)}$,
for $1\le s\le S$,
if $\text{dist}_{sk}^{(\ell)}>0$ for each $k=1,\ldots,K$, then set

$$u_{sk}^{(\ell)} \;=\; \frac{(\text{dist}_{sk}^{(\ell)})^{-\frac{1}{m-1}}}{\sum_{q=1}^{K}(\text{dist}_{sq}^{(\ell)})^{-\frac{1}{m-1}}}$$

otherwise set $u_{sk}^{(\ell)}=0$ for each k with $\text{dist}_{sk}^{(\ell)}>0$, and set

$$u_{sk}^{(\ell)} \;=\; \frac{1}{\|(\text{dist}_{sk}^{(\ell)})_k\|_0}$$

for each k with $\text{dist}_{sk}^{(\ell)}=0$.

Step 4. Compute new cluster centers $(\overline{D}_{j,i}^{k,(\ell+1)})_{k,j,i}$ based on weighted Euclidean means of the observations $(D_{j,i}^{s})_{s,j,i}$ as in Step 1., replacing the weight matrix $U^{(-1)}$ by the updated weight matrix $U^{(\ell)}$.

Step 5. Terminate when,

$$\sum_{k=1}^{K}\sum_{j=1}^{j_{\max}}\sum_{i=0}^{2^j-1}\|\overline{D}_{j,i}^{k,(\ell)}-\overline{D}_{j,i}^{k,(\ell+1)}\|_F^2<\epsilon$$

for some small value of ϵ, otherwise return to Step 2.

7.8 Proof of Proposition 4.1

Proof. Let U_π denote the (unitary) permutation matrix corresponding to the permutation $\pi(1,\ldots,d)$. For subject $s=1,\ldots,S$, let $(M_{1,i}^{s,\pi})_{i=0,1}$ be the midpoints at scale $j=1$ under the permuted ordering of the components. Also, let $(D_{j,i}^{s,\pi})_{j,i}$ be the thresholded pyramid of wavelet coefficients, with normalized variance, obtained under the permuted ordering of the components (using the permuted threshold vector $\sigma(\vec{\lambda})$). We verify that the permutation-invariance holds true in each step of the clustering algorithm in Section 4, described in more detail in Section 7.7.

- *Wavelet thresholding in Step 1.* By Proposition 3.6, the coarse-scale midpoints $(M_{1,i}^{s,\pi})_{i=0,1}$ and thresholded wavelet coefficients $(D_{j,i}^{s,\pi})_{j,i}$ satisfy:

$$M_{1,i}^{s,\pi} = U_\pi * M_{1,i}^{s}, \qquad \text{for all } s,i \tag{7.14}$$

$$D_{j,i}^{s,\pi} = U_\pi * D_{j,i}^{s}, \qquad \text{for all } s,j,i \tag{7.15}$$

- *Geometric fuzzy c-means algorithm in Step 2.* At iteration $\ell=0$, the distances $(\mathrm{dist}_{sk}^{(\ell)})_{s,k}$ and consequently the partition matrix $U^{(\ell)}$ are permutation-invariant, since for each s,k,

$$\mathrm{dist}_{sk}^{(\ell)} = \sum_{i=0}^{1}\delta\left(U_\pi * M_{1,i}^{s}, U_\pi * \overline{M}_{1,i}^{k,(\ell)}\right)^2 = \sum_{i=0}^{1}\delta\left(M_{1,i}^{s}, \overline{M}_{1,i}^{k,(\ell)}\right)^2$$

using that the Riemannian distance is invariant under congruence transformation by $U_\pi\in\mathcal{U}_d\subset \mathrm{GL}(d,\mathbb{C})$, and the fact that the initial cluster centers are randomly sampled from the permuted midpoints $(U_\pi * M_{1,0}^{s}, U_\pi * M_{1,1}^{s})_{s=1,\ldots,S}$ by eq.(7.14).

Both the empirical weighted Karcher mean in eq.(4.3) and its approximate version in eq.(4.4) based on the observations $(U_\pi * M_{1,i}^{s})_{s,i}$ and weights $(\mathrm{weight}_{sk}^{(\ell)})_{s,k}$ satisfy:

$$\overline{M}_{1,i}^{k,(\ell+1),\pi} = U_\pi * \overline{M}_{1,i}^{k,(\ell+1)}, \qquad \text{for } i=0,1$$

where $\overline{M}_{1,i}^{k,(\ell+1)}$ is the updated cluster center for cluster k under the non-permuted ordering of the components. This is easily verified by similar arguments as used in

the proof of Proposition 3.6.

Reiterating the above arguments, we observe that for each $\ell = 0, \ldots,$ the partition matrix $U^{(\ell)}$ is permutation-invariant and that the cluster centers satisfy $\overline{M}_{1,i}^{k,(\ell),\pi} = U_\pi * \overline{M}_{1,i}^{k,(\ell)}$. The termination criterion is also permutation-invariant, since:

$$\sum_{k=1}^{K}\sum_{i=0}^{1} \delta\left(U_\pi * \overline{M}_{1,i}^{k,(\ell)}, U_\pi * \overline{M}_{1,i}^{k,(\ell+1)}\right)^2 \;=\; \sum_{k=1}^{K}\sum_{i=0}^{1} \delta\left(\overline{M}_{1,i}^{k,(\ell)}, \overline{M}_{1,i}^{k,(\ell+1)}\right)^2$$

using again the congruence-invariance of the Riemannian distance function. We conclude that the partition matrix $U^{(L)}$, obtained at the final iteration of the fuzzy c-means algorithm under the permuted ordering of the components $\pi(1, \ldots, d)$, is exactly equivalent to the partition matrix obtained under the non-permuted ordering.

- *Weighted fuzzy c-means algorithm in Step 3.* At iteration $\ell = 0$, by eq.(7.15) and the fact that the partition matrix $U^{(-1)}$ is permutation-invariant, the (initial) cluster centers $(\overline{D}_{j,i}^{k,(\ell),\pi})_{k,j,i}$ satisfy:

$$\overline{D}_{j,i}^{k,(\ell),\pi} \;=\; U_\pi * \overline{D}_{j,i}^{k,(\ell)}, \qquad \text{for all } k, j, i$$

where $\overline{D}_{j,i}^{k,(\ell)}$ is the cluster center for cluster k under the non-permuted ordering of the components. The distances $(\mathrm{dist}_{sk}^{(\ell)})_{s,k}$ and consequently the partition matrix $U^{(\ell)}$ are permutation-invariant, as for each s, k,

$$\begin{aligned}\mathrm{dist}_{sk}^{(\ell)} &= \sum_{j=1}^{j_{\max}}\sum_{i=0}^{2^j-1} w_{jsk}\|U_\pi * D_{j,i}^{s} - U_\pi * \overline{D}_{j,i}^{k,(\ell)}\|_F^2 \\ &= \sum_{j=1}^{j_{\max}}\sum_{i=0}^{2^j-1} w_{jsk}\|D_{j,i}^{s} - \overline{D}_{j,i}^{k,(\ell)}\|_F^2\end{aligned}$$

since $U_\pi \in \mathcal{U}_d$ is a unitary matrix. Reiterating the same argument, we observe that for each $\ell = 0, \ldots,$ the partition matrix $U^{(\ell)}$ is permutation-invariant, and the cluster centers satisfy $\overline{D}_{j,i}^{k,(\ell),\pi} = U_\pi * \overline{D}_{j,i}^{k,(\ell)}$. Finally, the termination criterion is permutation invariant as:

$$\sum_{k=1}^{K}\sum_{j=1}^{j_{\max}}\sum_{i=0}^{2^j-1} \|U_\pi * \overline{D}_{j,i}^{k,(\ell)} - U_\pi * \overline{D}_{j,i}^{k,(\ell+1)}\|_F^2 \;=\; \sum_{k=1}^{K}\sum_{j=1}^{j_{\max}}\sum_{i=0}^{2^j-1} \|\overline{D}_{j,i}^{k,(\ell)} - \overline{D}_{j,i}^{k,(\ell+1)}\|_F^2$$

This proves that the partition matrix $U^{(L)}$, obtained at the final iteration of the weighted fuzzy c-means algorithm is invariant under the permuted ordering of the components of the time series $\pi(1, \ldots, d)$, and is exactly equivalent to the partition matrix obtained under the non-permuted ordering.

□

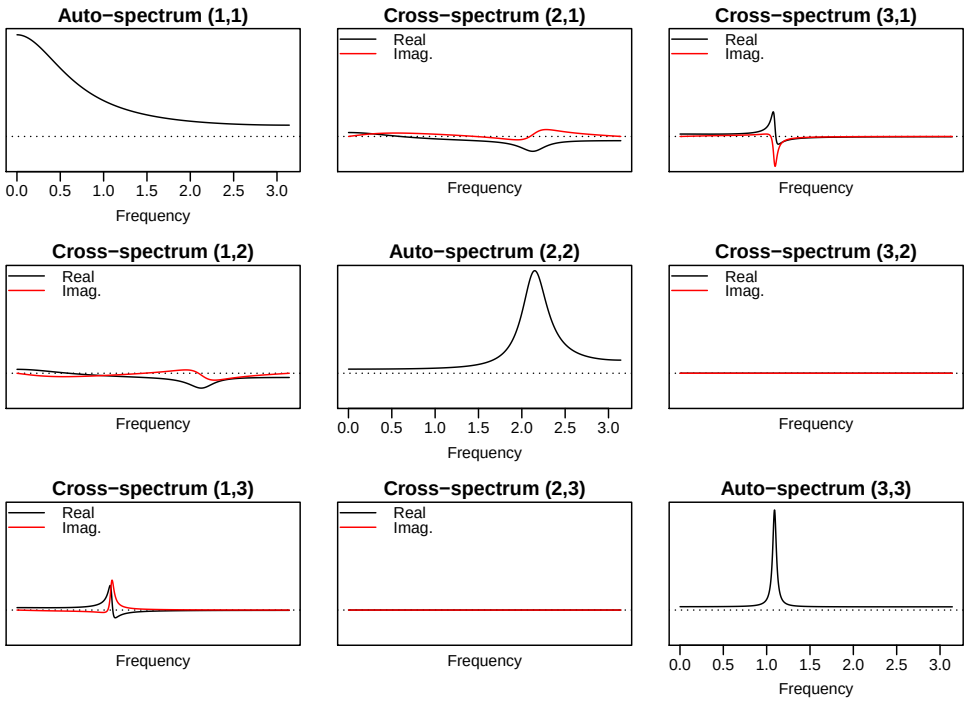

Figure 12: (3×3)-dimensional spectral matrix $f(\omega)$ at frequencies $\omega \in (0, \pi]$ with nonhomogeneous smoothness behavior across diagonal components of the spectral matrix.

8 Appendix B: additional simulated examples

To further illustrate the advantages of the developed spectral estimation framework towards smoothing or denoising of spectral matrices with nonhomogeneous smoothness behavior across components of the spectral matrix, we include several additional simulated examples based on artificially constructed spectral matrices. Figure 12 shows a (3×3)-dimensional Hermitian PD spectral matrix $f(\omega)$ at frequencies $\omega \in (0, \pi]$, where the componentwise smoothness behavior varies from a highly smooth curve over frequency in the auto-spectral component $(1, 1)$ to a localized peak in the auto-spectral component $(3, 3)$.

Consider the spectral matrix $f(\omega)$ at the Fourier frequencies $\omega_\ell = 2\pi\ell/T$, where the length of the time series T assumed to be even. We simulate multivariate stationary time series traces $\vec{Y}(t)$ with underlying spectrum $f(\omega_\ell)$ at the Fourier frequencies based on their Cramér representation, (see [3, Section 4.6]), through the inverse Fourier transform:

$$\vec{Y}(t) \quad = \quad \frac{1}{\sqrt{T}} \sum_{\ell=-(T/2-1)}^{T/2} f^{1/2}(\omega_\ell) \exp(it\omega_\ell)\vec{Z}_\ell, \qquad \text{for } t = 1, \ldots, T$$

where $f^{1/2}(\omega_\ell)$ is the Hermitian square root matrix of $f(\omega_\ell)$ and $\vec{Z}_\ell$ is a 3-dimensional complex standard normal random vector, such that $\vec{Z}_\ell = \vec{Z}^*_{-\ell}$ with $*$ the complex conjugate.

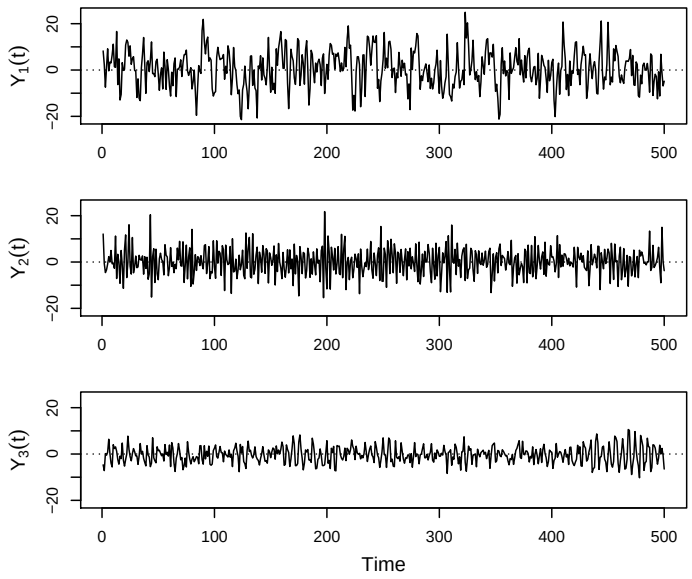

Figure 13: Simulated 3-dimensional stationary time series of length $T = 500$, with underlying spectrum $f(\omega_\ell)$ as in Figure 12.

For $\ell = 0$ and $T/2$; $\vec{Z}_\ell$ is a real standard normal random vector. Figure 13 shows a simulated 3-dimensional time series trace with underlying spectrum $f(\omega_\ell)$ at the Fourier frequencies. Given the simulated time series, we compute benchmark multitaper spectral estimates, see e.g. [28], based on Slepian (also called Discrete Prolate Spheroidal) tapering functions using the tools in the `R`-package `multitaper` available on CRAN, [16]. As shown in Figure 14, considering a small number of Slepian tapering functions the multitaper spectral estimate captures the localized peak in auto-spectral component $(3, 3)$, but is highly noisy in the other components of the estimated spectral matrix. On the other hand, as observed in Figure 15, selecting a very large number of Slepian tapers, the multitaper spectral estimate captures the smooth behavior in auto-spectral component $(1, 1)$ but smooths out the localized peaks and troughs. In contrast, Figure 16 shows the wavelet-thresholded spectral estimate, which captures both the smooth behavior in auto-spectral component $(1, 1)$ and the localized peak in auto-spectral component $(3, 3)$. The initial highly noisy spectral estimate before wavelet thresholding is based on a multitaper spectral estimate with $B = d = 3$ Slepian tapers to guarantee positive-definiteness, and the automatic wavelet threshold is selected by cross-validation (as described in Section 3). The tools to compute the wavelet-thresholded spectral estimator are provided by the `R`-package `pdSpecEst` available on CRAN, [4].

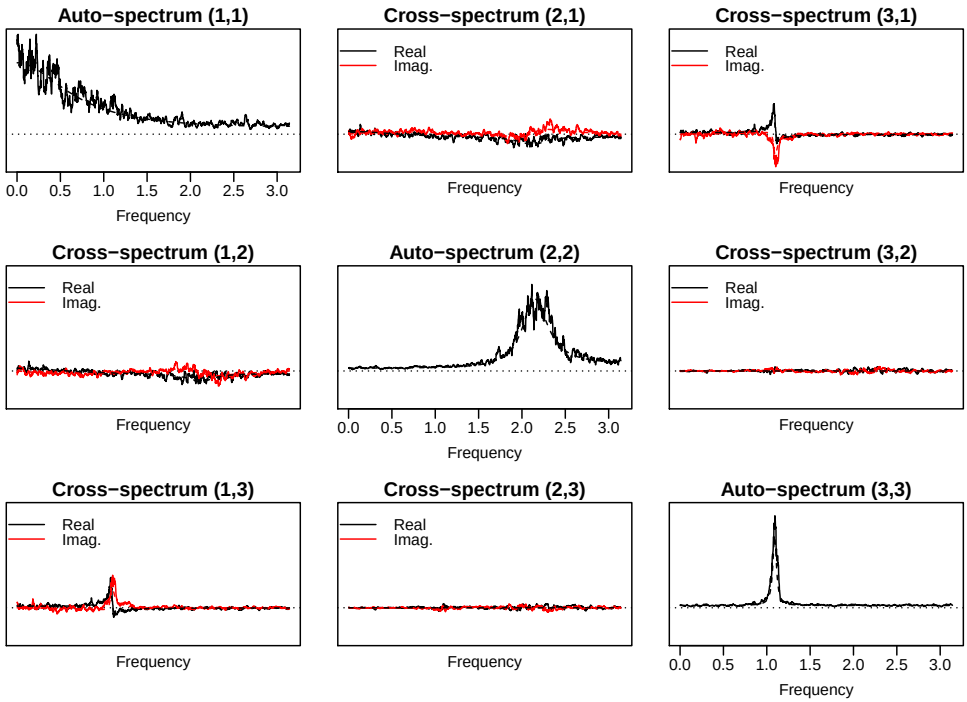

Figure 14: Benchmark multitaper spectral estimate (continuous line) with $B = 20$ Slepian tapers for a time series trace of length $T = 2^{12}$ and true underlying spectrum (dashed line).

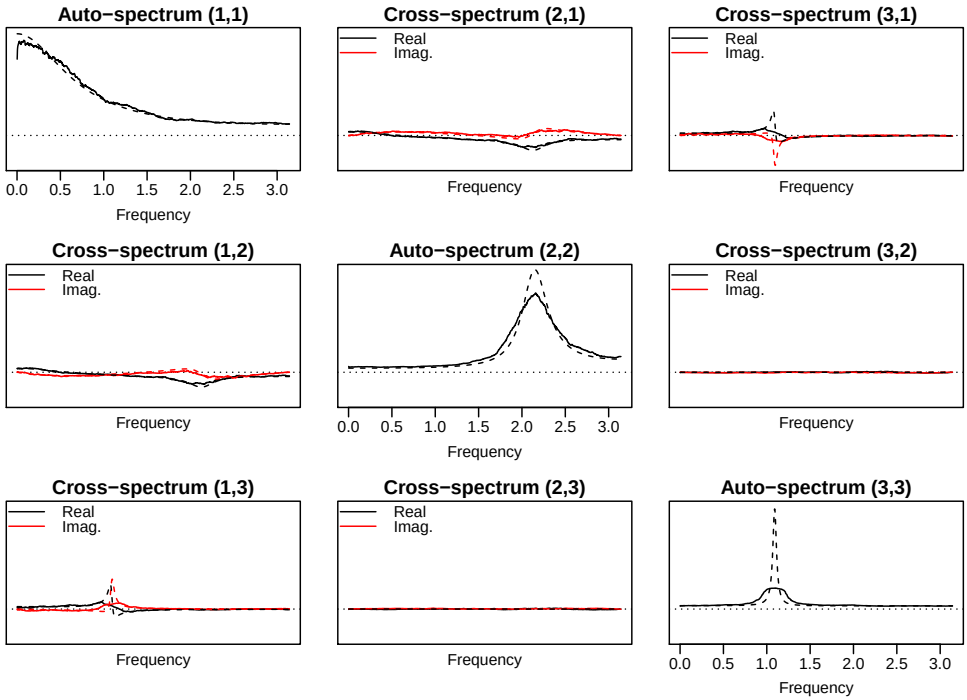

Figure 15: Benchmark multitaper spectral estimate (continuous line) with $B = 500$ Slepian tapers for a time series trace of length $T = 2^{12}$ and true underlying spectrum (dashed line).

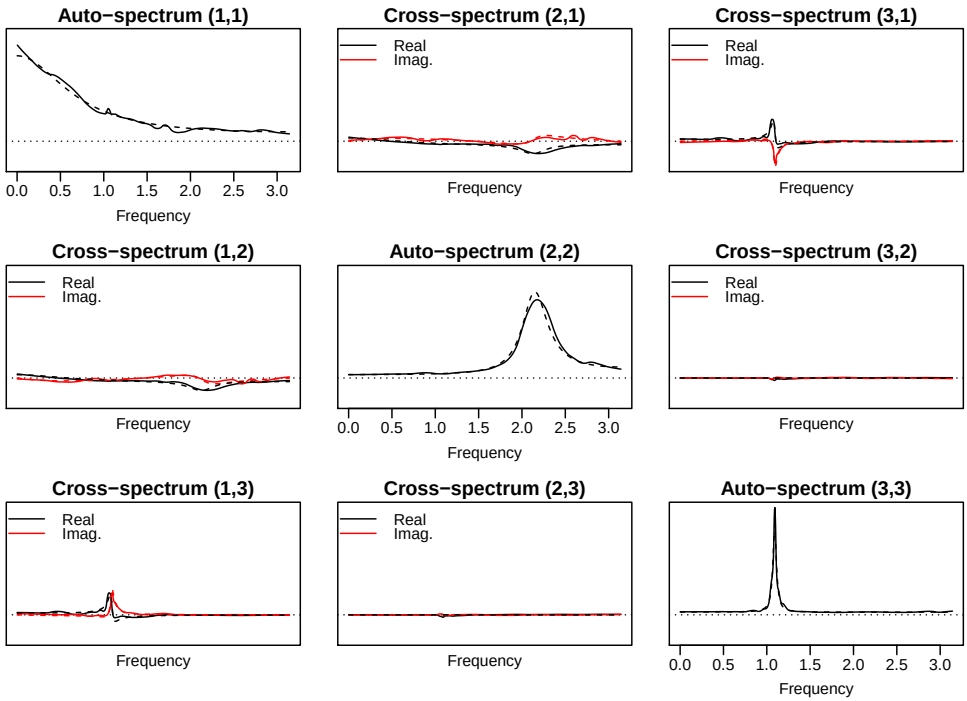

Figure 16: Automatic wavelet-thresholded spectral estimate (continuous line) for a time series trace of length $T = 2^{12}$ and true underlying spectrum (dashed line).

References

[1] J.C. Bezdek. *Pattern Recognition with Fuzzy Objective Function Algorithms*. Plenum Press, New York, 1981.

[2] R. Bhatia. *Positive Definite Matrices*. Princeton University Press, New Jersey, 2009.

[3] D.R. Brillinger. *Time Series: Data Analysis and Theory*. Holden-Day, San Francisco, 1981.

[4] J. Chau. *pdSpecEst: Positive-Definite Wavelet-Based Multivariate Spectral Analysis*, 2017. R package version 1.0.0.

[5] J. Chau and R. von Sachs. Functional mixed effects wavelet estimation for spectra of replicated time series. *Electronic Journal of Statistics*, 10(2):2461–2510, 2016.

[6] R. Dahlhaus. *Locally stationary processes*, chapter in Time Series Analysis: Methods and Applications, Vol. 30, pages 351–413. Elsevier B.V., Amsterdam, 2012.

[7] M. Dai and W. Guo. Multivariate spectral analysis using Cholesky decomposition. *Biometrika*, 91(3):629–643, 2004.

[8] M.P. do Carmo. *Riemannian Geometry*. Birkhäuser, Boston, 1992.

[9] D.L. Donoho. *Smooth wavelet decompositions with blocky coefficient kernels*, chapter in Recent Advances in Wavelet Analysis, pages 259–308. Academic Press, New York, 1993.

[10] M. Fiecas and H. Ombao. Modeling the evolution of dynamic brain processes during an associative learning experiment. *Journal of the American Statistical Association*, 111(516):1440–1453, 2016.

[11] C. Gorrostieta, H. Ombao, R. Prado, S. Patel, and E. Eskandar. Exploring dependence between brain signals in a monkey during learning. *Journal of Time Series Analysis*, 33(5):771–778, 2012.

[12] J. Ho, G. Cheng, H. Salehian, and B.C. Vemuri. Recursive karcher expectation estimators and recursive law of large numbers. *AISTATS*, pages 325–332, 2013.

[13] M. Jansen. *Noise Reduction by Wavelet Thresholding.* Springer-Verlag, New York, 2001.

[14] M. Jansen and P. Oonincx. *Second Generation Wavelets and Applications.* Springer-Verlag, London, 2005.

[15] Y. Kakizawa, R.H. Shumway, and M. Taniguchi. Discrimination and clustering for multivariate time series. *Journal of the American Statistical Association*, 93(441):328–340, 1998.

[16] R. Karim and W.S. Burr. *multitaper: Multitaper Spectral Analysis Tools*, 2016. R package version 1.0-12.

[17] R.T. Krafty and W.O. Collinge. Penalized multivariate Whittle likelihood for power spectrum estimation. *Biometrika*, pages 1–12, 2013.

[18] R.J. Muirhead. *Aspects of Multivariate Statistical Theory.* John Wiley & Sons, New Jersey, 1982.

[19] G.P. Nason. Wavelet shrinkage using cross-validation. *Journal of the Royal Statistical Society: Series B*, pages 463–479, 1996.

[20] X. Pennec. Intrinsic statistics on Riemannian manifolds: Basic tools for geometric measurements. *Journal of Mathematical Imaging and Vision*, 25(1):127–154, 2006.

[21] X. Pennec, P. Fillard, and N. Ayache. A Riemannian framework for tensor computing. *International Journal of Computer Vision*, 66(1):41–66, 2006.

[22] I.U. Rahman, I. Drori, V.C. Stodden, D.L. Donoho, and P. Schröder. Multiscale representations for manifold-valued data. *Multiscale Modeling & Simulation*, 4(4):1201–1232, 2005.

[23] O. Rosen and D.S. Stoffer. Automatic estimation of multivariate spectra via smoothing splines. *Biometrika*, 94(2):335–345, 2007.

[24] S.T. Smith. Intrinsic Cramér-Rao bounds and subspace estimation accuracy. In *Proceedings of the IEEE Sensor Array and Multichannel Signal Processing Workshop*, pages 489–493. IEEE, 2000.

[25] G.C. Tseng. Penalized and weighted K-means for clustering with scattered objects and prior information in high-throughput biological data. *Bioinformatics*, 23(17):2247–2255, 2007.

[26] A.M. Tulino and S. Verdú. *Random Matrix Theory and Wireless Communications*. Now Publishers Inc., Hanover, 2004.

[27] G. Wahba. Automatic smoothing of the log periodogram. *Journal of the American Statistical Association*, 75(369):122–132, 1980.

[28] A.T. Walden. A unified view of multitaper multivariate spectral estimation. *Biometrika*, 87(4):767–788, 2000.